

AFIT/GAE/ENY/99M-07

**HEAT TRANSFER TO THE INCLINED
TRAILING WALL OF AN OPEN CAVITY**

THESIS

**Orval A. Powell, B.S.
Second Lieutenant, USAF**

AFIT/GAE/ENY/99M-07

Approved for public release; distribution unlimited

THIS QUALITY INSPECTED 3

19990409 060

REPORT DOCUMENTATION PAGE			Form Approved OMB No. 0704-0188	
Public reporting burden for this collection of information is estimated to average 1 hour per response, including the time for reviewing instructions, searching existing data sources, gathering and maintaining the data needed, and completing and reviewing the collection of information. Send comments regarding this burden estimate or any other aspect of this collection of information, including suggestions for reducing this burden, to Washington Headquarters Services, Directorate for Information Operations and Reports, 1215 Jefferson Davis Highway, Suite 1204, Arlington, VA 22202-4302, and to the Office of Management and Budget, Paperwork Reduction Project (0704-0188), Washington, DC 20503.				
1. AGENCY USE ONLY (Leave blank)	2. REPORT DATE March 1999	3. REPORT TYPE AND DATES COVERED Master's Thesis		
4. TITLE AND SUBTITLE HEAT TRANSFER TO THE INCLINED TRAILING WALL OF AN OPEN CAVITY		5. FUNDING NUMBERS		
6. AUTHOR(S) Orval A. Powell, 2Lt, USAF				
7. PERFORMING ORGANIZATION NAME(S) AND ADDRESS(ES) Air Force Institute of Technology 2950 P Street WPAFB, OH 45433-7765		8. PERFORMING ORGANIZATION REPORT NUMBER AFIT/GAE/ENY/99M-07		
9. SPONSORING/MONITORING AGENCY NAME(S) AND ADDRESS(ES) Dr. James Weber, Civilian, Program Director High-Speed Systems Development Branch, AFRL/PRSS 1790 Loop Rd North WPAFB, OH 45433		10. SPONSORING/MONITORING AGENCY REPORT NUMBER		
11. SUPPLEMENTARY NOTES Jeffrey P. Bons, Capt, USAF (937) 255-3636 ext 4643 jeffrey.bons@afit.af.mil				
12a. DISTRIBUTION AVAILABILITY STATEMENT Distribution unlimited		12b. DISTRIBUTION CODE		
13. ABSTRACT (Maximum 200 words) Experimental and computational heat transfer investigations were performed on a cavity with an inclined trailing wall (20-degrees to the horizontal), simulating one under investigation for use in a scramjet engine. Heat transfer data are reported in the form of Stanton number obtained using a curve fit to the recorded transient surface temperature history under cold flow conditions. Ascending from the reattachment point, the Stanton number increased by nearly 50% due to flow compression. This effect of flow compression was also evident at the junction of the cavity floor and inclined trailing wall, where the Stanton number also increased by 50%. Descending from the reattachment point, the Stanton number increased by 30% due to flow recirculation. Downstream of the inclined trailing wall, the Stanton number increased by 90% due to the boundary layer-shock interaction when compared to that at the same axial location on a flat plate. A schlieren flow visualization technique was employed, showing the formation of the oblique shock from coalescing weak compression waves. For comparison, a 2-D Navier-Stokes CFD analysis was performed using a realizable k-epsilon turbulence model. In the cavity, the CFD Stanton number results were an order of magnitude lower than the experimental values, while downstream of the cavity, the CFD Stanton number results were 40% lower than the experimental results. Similar differences are noted within the open literature with application of various turbulence models, suggesting that the flow in the cavity is quite complex and the use of two equation turbulence models requires closer investigation.				
14. SUBJECT TERMS convection(heat transfer), cold flow, computational fluid dynamics, flame holders, supersonic combustion ramjet engines			15. NUMBER OF PAGES 110	
			16. PRICE CODE	
17. SECURITY CLASSIFICATION OF REPORT Unclassified	18. SECURITY CLASSIFICATION OF THIS PAGE Unclassified	19. SECURITY CLASSIFICATION OF ABSTRACT Unclassified	20. LIMITATION OF ABSTRACT UL	

Disclaimer

The views expressed in this thesis are those of the author and do not reflect the official policy or position of the United States Air Force, the Department of Defense, or the United States Government.

AFIT/GAE/ENY/99M-07

HEAT TRANSFER TO THE INCLINED TRAILING WALL OF AN OPEN CAVITY

THESIS

Presented to the Faculty of the Graduate School of Engineering of the

Air Force Institute of Technology

Air University In Partial Fulfillment of the

Requirements for the Degree of

Master of Science in Aeronautical Engineering

Orval A. Powell, B.S.

Second Lieutenant, USAF

Air Force Institute of Technology

Wright-Patterson AFB, Ohio

March 1998

Sponsored in part by Dr. James Weber, Program Manager, High-Speed Systems Development
Branch, AFRL/PRSS

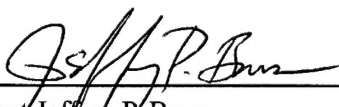
Approved for public release; distribution unlimited

HEAT TRANSFER TO THE INCLINED TRAILING WALL OF AN OPEN CAVITY

Orval A. Powell, B.S.


Second Lieutenant, USAF

Approved:



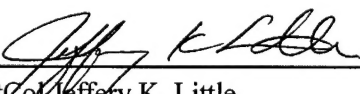
Capt Jeffrey P. Bons
Committee Chairman

8 Mar 99
Date



Dr. Milton E. Franke
Committee Member

8 Mar 99
Date



LtCol Jeffery K. Little
Committee Member

8 Mar 99
Date

Acknowledgments

I would like to thank several people for the time and attention they afforded either me or this work. Thanks to the Lord above, who guided me with the serenity and wisdom to persevere and reach this goal, while also watching over me on several remarkable instances. My sincere appreciation goes to my advisor, Capt. Jeffrey Bons who gladly became my advisor, even though this work was not in his research area. Furthermore, he addressed my multitude of questions by always providing direction and instruction without giving me the answer. This, at times, increased my stress level, but made this work that much more meaningful. I also extend a great deal of thanks to Mr. Andrew Pitts who was always open to questions and last minute changes. His technical expertise and sense of humor saw me through several difficult times. To Mr. Jan LeValley and Mr. Condie Inman of the AFIT Model Shop, who produced an exceptional model correctly and ahead of schedule, despite my rather crude drawings. They also made many modifications while I waited, which allowed me to continue my work with little delay.

My deepest appreciation and gratitude go to my wife, Aimée, and daughter, Jorin. Aimée always stood by me with encouraging words and loving glances despite my long hours of homework and thesis work, while Jorin's smile and laughter always warmed my heart. With love and admiration, I thank you both - I couldn't have done this without you.

Orval A. Powell

Table Of Contents

	Page
Acknowledgments	vi
Table Of Contents	vii
List of Figures	x
List of Tables	xii
List of Symbols	xiii
Abstract	xviii
Chapter 1. INTRODUCTION	1
1.1 Motivation	1
1.2 Problem Statement	2
1.3 Summary of Current Knowledge	3
1.4 Present Work	5
1.5 Outline	5
Chapter 2. BACKGROUND	7
2.1 Navier-Stokes Equations	7
2.2 Nondimensional Parameters	11
2.2.1 Reynolds Number, Re	11
2.2.2 Eckert Number, Ec	11
2.2.3 Mach Number, M	12

2.2.4	Prandtl Number, Pr	12
2.2.5	Stanton Number, St	12
2.2.6	Grashof Number, Gr	14
Chapter 3. EXPERIMENTAL FACILITIES		16
3.1	Wind Tunnel Facilities	16
3.1.1	Plenum Chamber	16
3.1.2	Mach 2.9 Nozzle	17
3.2	Measurement Equipment	17
3.2.1	Data Acquisition	19
3.2.2	Flow Visualization	19
3.3	Cavity Geometry	21
3.3.1	Cavity Design	22
3.3.2	Cavity Assembly	33
3.3.3	Cavity Hardware	34
3.4	Experimental Procedure	35
3.5	Data Reduction	35
Chapter 4. COMPUTATIONAL SETUP		41
4.1	Computational Facilities	41
4.2	Software Inputs	41
4.2.1	Solver Settings	41

4.2.2	Boundary Conditions	43
4.3	Grid Generation	43
4.4	Parameter Calculation	47
4.5	Code Validation	47
Chapter 5.	RESULTS AND DISCUSSION	48
5.1	Experimental Results	48
5.1.1	Thermocouple Data	48
5.1.2	Shock Placement	51
5.1.3	Stanton number correlation	54
5.2	Computational Results	61
5.2.1	Flat Plate Insert	61
5.2.2	Inclined Trailing Wall Insert	61
5.3	Experimental and Computational Comparisons	70
Chapter 6.	CONCLUSIONS AND RECOMMENDATIONS	76
6.1	Conclusions	76
6.2	Recommendations	79
Appendix A.	UNCERTAINTY ANALYSIS	81
Bibliography	83
Vita	87

List of Figures

	Page
Figure 1. Control volume around cavity surface	13
Figure 2. Schematic of AFIT's Mach 2.9 wind tunnel	17
Figure 3. Schematic of half nozzle and test section	18
Figure 4. Schematic of schlieren setup	20
Figure 5. Schematic showing density gradient across oblique shock	21
Figure 6. Placement of thermocouples in cavity insert	29
Figure 7. Final cavity geometry	31
Figure 8. Placement of cavity insert attachment bolts	32
Figure 9. Schematic of cavity inserts and negatives of upper surfaces	33
Figure 10. Comparison between fit and recorded data for flat plate; station 1	36
Figure 11. Determination of corrected temperature amplitude	38
Figure 12. Forward section of grid for flat plate CFD model	44
Figure 13. Grid and computational domain for cavity with inclined trailing wall	45
Figure 14. Closeup of cavity grid	46
Figure 15. Comparison between fit and recorded data for inclined trailing wall; station 5	49
Figure 16. Schlieren photograph showing flow reattachment and oblique shock formation	52

	Page
Figure 17. Integral values along inclined trailing wall; taken from Horstman <i>et al.</i> [17]	53
Figure 18. Displacement thickness along inclined trailing wall; CFD results	55
Figure 19. Stanton number variation with axial position for inclined trailing wall and flat plate inserts; experimental results	56
Figure 20. Comparison between predicted and recorded temperature histories for flat plate insert; station 1	59
Figure 21. Stanton number variation with axial position for flat plate; CFD results	62
Figure 22. Pressure distribution through cavity; CFD results	63
Figure 23. Mach number distribution through cavity; CFD results	64
Figure 24. Static temperature distribution through cavity; CFD results	65
Figure 25. Stanton number variation with axial position; CFD results	66
Figure 26. Velocity vectors through cavity; CFD results	68
Figure 27. Skin friction coefficient variation along inclined trailing wall	69
Figure 28. Comparison of Stanton number for flat plate insert; CFD and experimental results	71
Figure 29. Comparison of Stanton number for inclined trailing wall; CFD and experimental results	72

List of Tables

	Page
Table 1. Matched parameter comparison	22
Table 2. Cavity geometry comparison	26
Table 3. Thermocouple station labels	28
Table 4. Test conditions	48
Table 5. Comparison of results with the literature	73
Table 6. Turbulence models used to examine cavity flows	74
Table 7. Uncertainty analysis for Stanton number calculation; station 5	82

List of Symbols

English Symbols

Symbol	Definition
a	Speed of sound (m/s)
A	Temperature amplitude (K , see equation (48))
c_f	Local coefficient of friction (see equation (41))
$c_{f\infty}$	Skin friction coefficient
c_p	Specific heat at constant pressure ($J/(kgK)$)
c_v	Specific heat at constant volume ($J/(kgK)$)
C_f	Total coefficient of friction (see equation (42))
d	Diameter (m)
D_h	Hydraulic diameter (m)
Ec	Eckert number
f	Focal length (m)
g	Earth's gravitational constant ($9.81 m/s^2$)
Gr	Grashof number
h	Specific enthalpy (J/kg)
h	Heat transfer coefficient (W/m^2)
k	Thermal conductivity ($W/(mK)$)
L	Length (m)
M	Mach number
p	Pressure (Pa)
Pr	Prandtl number

q''	Heat transfer flux (W/m^2)
r	Recovery ratio
R	Gas constant for air ($J/(kgK)$)
R	Measured quantity
Re	Reynolds number
RMS	Root mean square
St	Stanton number
t	Time (sec)
T	Temperature (K)
u	x-direction velocity (m/s)
v	y-direction velocity (m/s)
V	Velocity (m/s)
w	Error bound
x	Distance (m)
x	x -direction
y	y -direction
y^+	Wall coordinate (m)

Greek Symbols

Symbol	Definition
α	Absorptivity
α	Thermal diffusivity (m^2/s)
β	Shock angle ($degrees$)
β	Volumetric thermal expansion coefficient (K^{-1})

δ	Boundary layer thickness (m)
δ^*	Displacement thickness (m)
Δ	Difference
ε	Emissivity
γ	Ratio of specific heats (c_p/c_v)
λ	Second viscosity coefficient (Ns/m^2)
μ	Dynamic (absolute) viscosity (Ns/m^2)
ν	Kinematic viscosity (m^2/s)
ρ	Density (kg/m^3)
ρ	Reflectivity
π	Constant (3.14159)
θ	Momentum thickness (m)
τ	Shear stress (Pa)
ω	Frequency (rad/sec)
ω	Power law exponent for Sutherland's equation (see equation (39))

Subscripts

Symbol	Definition
∞	Freestream
0	Stagnation
<i>ave</i>	Average
<i>aw</i>	Adiabatic wall
<i>cond</i>	Conduction
<i>conv</i>	Convection

<i>corr</i>	Corrected
D_h	Hydraulic diameter
<i>f</i>	Film
<i>fit</i>	Curve fit
<i>i</i>	Initial
<i>L</i>	Based on <i>L</i>
<i>plexi</i>	Plexiglas
<i>pred</i>	Predicted
<i>rad</i>	Radiation
<i>rec</i>	Recorded
<i>ref</i>	Reference value
<i>R</i>	Measured quantity
<i>t</i>	Time
<i>t</i>	Turbulent
<i>w</i>	Wall
<i>x</i>	Based on <i>x</i>

Superscript

Symbol	Definition
$\overline{()}$	Mean value of Reynolds-averaged variable
$()'$	Fluctuating value of Reynolds-averaged variable
*	Nondimensional value

Abbreviations

Abbreviation	Definition
2-D	Two dimensional
3-D	Three dimensional
A/D	Analog-digital convertor
AFIT	Air Force Institute of Technology
cw	Clockwise
ccw	Counter-clockwise
CFD	Computational Fluid Dynamics
Exp	Experimental
Hyper-X	Hypersonic Experimental Research Vehicle
HyTech	Hypersonics Technology Program
LE	Leading edge
n/a	Not applicable
PC	Personal computer
scramjet	Supersonic combustion ramjet
SI	Système International d'Unités
TC	Thermocouple

Abstract

An experimental and computational investigation of a cavity geometrically similar to one currently being investigated for use in a supersonic combustion ramjet (scramjet) engine was performed in a cold flow environment without fuel addition. The cavity has an inclined trailing wall and serves two functions: increase the residence time of the fuel/air mixture in the combustion chamber and act as a flame holder. Due to the use of cold flow, the current work forms a baseline case on which future, more sophisticated experimentation can build.

The current work determined the axial variation of heat transfer in the form of Stanton number using temperature data recorded along the walls of a driven cavity. These results were compared to Stanton number calculations from recorded temperature data along a flat plate at two axial locations. From the experimental data, the Stanton number downstream of the cavity was found to be 90% higher than that of the flat plate at the same axial location. This suggests that the responsible physical mechanism was the boundary layer-shock interaction at the top of the inclined trailing wall. Again from the experimental data, the Stanton number in the base of the cavity was 8% lower than that of the flat plate at the same axial location, suggesting that the decrease was due to flow recirculation within the cavity. Along the inclined trailing wall, the Stanton number varied depending on position from the reattachment point. Descending the inclined wall from that point, the Stanton number increased 30% from the value near reattachment. This result suggests that flow recirculation with its associated changing fluid velocity and direction was the responsible physical mechanism. Ascending the inclined wall from the reattachment point, the Stanton number increased nearly 50% from the value near reattachment. The increase suggests that the conversion of kinetic energy to thermal energy was the responsible physical mechanism. The conversion of

energy was due to the flow turning at the inclined trailing wall. This flow turning was also seen at the cavity floor inclined trailing wall junction. The Stanton number on the cavity floor was 50% higher than that just removed up the inclined wall. Relative to the flow descending the inclined wall, the floor represented a wedge that abruptly turned the flow, resulting in the above mentioned conversion of energy. For comparison, a two dimensional Navier-Stokes computational evaluation was performed using a realizable $k - \epsilon$ turbulence model to account for the closure problem. Although varying in magnitude, the CFD results displayed a similar trend in Stanton number along the inclined trailing wall as the experimental results. In the base of the cavity, the CFD Stanton number results were an order of magnitude lower than the experimental values, while downstream of the cavity, the CFD Stanton number results were 40% lower than the experimental results. Similar differences are noted within the open literature with application of various turbulence models, suggesting that the flow in the cavity is quite complex and the use of two equation turbulence models requires closer investigation.

HEAT TRANSFER TO THE INCLINED TRAILING WALL OF AN OPEN CAVITY

Chapter 1 - Introduction

1.1 Motivation

Although hypersonic flight is not a new field of study, it is a field that is still in its early development due to political and budget considerations during the 1950's and 1960's. These considerations halted progress when interest in the field was in the forefront [26]. Recent programs, such as the National Aerospace Plane, Hyper-X and HyTech, have brought about a resurgence of interest in hypersonic technology. With this resurgence, there has been a great deal of research in all areas associated with hypersonic flight, from material design to thermal management to propulsion. Though all of these areas have seen considerable research activity, the propulsion system has been a focal point of a great deal of research. This concentration is due in part to the results of past work, such as the X-15 project, which achieved sustained flight at Mach 6.7 using a rocket propulsion system [26]. However, this flight Mach number cannot be attained efficiently with current air-breathing ramjet engines.

The limit of a ramjet propulsion system is about Mach 6 because of incomplete combustion due to extremely high air temperatures [16]. Current research programs, such as Hyper-X and HyTech, are striving for Mach numbers in excess of Mach 6 from an air-breathing propulsion system. The use of air is critical since the oxidizer need not be carried on-board as in a rocket propulsion system, thereby lowering the required weight of the vehicle. Although at this flight speed,

engine combustion occurs in a supersonic flow, with residence times on the order of a millisecond or less [16]. These short residence times will hinder or prevent complete mixing and combustion.

In spite of these short residence times, the successful design of a scramjet propulsion system is considered to be the key to achieving sustained hypersonic flight [26]. This is due to the fact that a scramjet propulsion system is a large part of the vehicle design, since airbreathing hypersonic propulsion systems are integral to the vehicle's airframe [26, 29].

1.2 Problem Statement

The goal of the HyTech program is to demonstrate the performance and operability of a Mach 4-8 hypersonic scramjet propulsion system that will operate on a storable hydrocarbon-fueled vehicle [29]. To this end, the program is examining the various components of scramjet propulsion.

As mentioned above, the residence time of the fuel/air mixture in the combustor is an area of particular concern with regard to the construction of a viable, functioning scramjet propulsion system. The HyTech program is evaluating the use of a recessed flame holder (cavity) to increase fuel-air mixing and residence times in the combustion chamber [10, 11]. In fact, fuel-air mixing "...has been a major feasibility problem in the design of [scramjet] combustors" [4]. While the use of the cavity affords low total pressure losses, there are high heat loads present in the cavity [10]. The trailing wall of this cavity results in a stagnation region for the freestream flow, causing the flow to recirculate within the cavity [33]. This recirculation causes the cavity to act as a flameholder which, in turn, will allow the flow to reside in the combustion chamber over a longer period of time than without the cavity. The stagnation region caused by the trailing wall is also a significant drawback of this design. A stagnation region is a source of high heat transfer rates in any flow due to the large velocity gradients through the boundary layer. The result is a substantial conversion of kinetic energy to thermal energy [21]. Current research has advanced active cooling technology,

(such as the use of endothermic fuels), to a level that should be able to endure the high heat loads that will be present in a scramjet propulsion engine [10]. However, the amount of experimental data pertaining to heat loading in a cavity flow is limited. This is significant considering the use of fuel as an active coolant and the fact that hydrocarbon fuels have a limited cooling capability [39]. Therefore, the aim of the present research was to extend the cavity flow heat flux data base and to increase the physical understanding of this complex flowfield.

1.3 Summary of Current Knowledge

Both cold and hot flow tests have been conducted to gain more insight into the flow characteristics of a scramjet propulsion system. Cold flow tests, as the name suggests, do not involve fuel combustion and generally involve use of air at a low temperature, typically much lower than the operational level. Hot flow tests use a temperature corresponding to the desired flight conditions and may or may not involve fuel combustion. As one might imagine, cold flow tests are much less expensive and generally provide a starting point for research.

In terms of scramjet propulsion systems, cold flow tests have been performed because of thermal management issues, as well as increased complexity, surrounding hot flow tests. Cold flow tests are a convenient and quick way to test various components before use in a hot flow test [3]. This was echoed at a recent workshop among Air Force and NASA colleagues who are conducting research on supersonic combustion [39]. As discussed in this reference, it's desirable to match flight properties, such as Mach number, Reynolds number and stagnation temperature and pressure, as closely as possible. However, the increased cost and complexity associated with high pressure systems, air heating systems and facility cooling necessitate the need for cold flow tests. For example, Orth and Cameron [27] discuss the experimental results of a cold flow test to evaluate the flow field behind a rear facing step in a scramjet combustor with fuel injection at the top of the

rear facing step. A cold flow test was useful in this case since fuel injection was the item of interest. As will be evident later, this geometry differs from the present research because a trailing wall was not employed.

Computational cold flow studies have also been performed. Alfahaid *et al.* [2] sought to validate a computational code by comparing the computational results to data from experimental testing of stacked injectors in a simulated scramjet combustor. The result was that the computational solution and experimental data were in good overall agreement. Thus, cold flow experimental data can be used to validate a computational model before modifying it for hot flow simulation. The results from the hot flow computational model could be used to construct an experimental hot flow test. This design process of modeling or testing using cold flow is utilized elsewhere as well. McConnaughey and Andrews [23] discuss that "...[computational modeling] and cold flow testing are a critical part of advanced propulsion technology..." for use in full-scale development of test hardware. These cold flow tests and computational models provide "initial concepts or baseline designs." Furthermore, computational models or cold flow tests can be scaled to determine or predict hot flow performance.

In an effort to limit the negative effects of a cavity while maintaining the desired flow field effects, an inclined trailing wall has been suggested by Davis and Bowersox [10]. Their research examined the effectiveness of this cavity geometry to act as a flame holder and to increase the fuel/air residence time in the combustion chamber. The conclusion was that a cavity containing an inclined trailing wall was beneficial in terms of increasing fuel/air residence time.

Research involving inclined trailing cavity walls is not new. Horstman *et al.* [17] and Settles *et al.* [33] examined the effect of a reattaching free shear layer on an inclined trailing wall at $M_\infty = 2.92$. However, heat transfer rates to this inclined trailing wall were not measured. Instead, the skin friction coefficient was measured.

As one might suspect, heat transfer rates are already high in actual scramjet combustors without adding the effects of a stagnation region in a cavity. These high heat transfer rates are directly related to the high stagnation temperatures associated with high Mach number flight. Using actual photographs, Stouffer [36] describes how wall heat transfer rates were so high in past scramjet ground based testing that the combustor side walls actually melted. However, the problem of dealing with these high heat transfer rates is not new. The open literature contains several reports detailing the thermal management considerations of scramjet combustion. Cold flow evaluation of components has been used prior to use in hot flow tests [3], as discussed above. Weckesser [45], for example, discusses how the high stagnation temperature and high shear, coupled with the oxidizing atmosphere present in the scramjet combustor and inlet section have greatly increased the need for material thermal management. This observation is just as accurate today because heat transfer rates in scramjet engines are still significant. Dealing with these high heat transfer rates is the focus of considerable research.

1.4 Present Work

The present work makes use of an inclined (20° to the horizontal) trailing wall in a cavity similar to that used in the literature [33], and in current HyTech research [10] (see Figure 7). The air flow separates over the cavity leading edge, thus forming a free shear layer before reattachment on the inclined trailing wall. The wall downstream of the cavity was at the same height as the wall upstream of the cavity. The cavity cold flow tests were performed at a stagnation temperature of 295 K and a stagnation pressure of $2.87E5\text{ Pa}$ in AFIT's Mach 2.9 wind tunnel.

1.5 Outline

This section provides an overview of the chapters to follow. Chapter 2 contains a discussion of the equations and nondimensional parameters relevant to the current work. A discussion

of the experimental facilities, including wind tunnel hardware, flow visualization equipment, cavity geometry, test procedures and data reduction is included in Chapter 3. Chapter 4 contains a discussion of the computational facilities, including boundary conditions, software inputs and grid generation. The results of the experimental and computational Stanton number data are presented and compared in Chapter 5. This chapter also contains a comparison of the flow structure from schlieren photography and computational results. Finally, Chapter 6 contains a series of conclusions and recommendations for future work.

An appendix is also included, Appendix A, containing an uncertainty analysis of the Stanton number calculation for the center position of the inclined trailing wall.

Chapter 2 - Background

This chapter contains information regarding the governing fluid equations, a nondimensionalization of these equations and a discussion of the relevant nondimensional parameters.

2.1 Navier-Stokes Equations

The Navier-Stokes equations are the governing equations for the fluid flow in the simulated scramjet cavity. For newtonian fluids using Stokes' hypothesis ($\lambda + \frac{2}{3}\mu = 0$), the three equations for momentum are named the Navier-Stokes equations. However, it has become common practice to refer to the collection of continuity, momentum and energy equations as the Navier-Stokes equations. This practice will be continued throughout this thesis. The equations were developed for steady, compressible, two dimensional turbulent boundary layer flow with no suction or blowing at the wall. The same order-of-magnitude considerations used in laminar boundary layer developments were used here [21, 49], with the additional assumption that all fluctuating terms are small compared to the mean values [49]. With these guidelines, the Navier-Stokes equations become:

Continuity

$$\frac{\partial}{\partial x}(\bar{\rho} \bar{u}) + \frac{\partial}{\partial y}(\bar{\rho} \bar{v}) = 0 \quad (1)$$

x-momentum

$$\bar{\rho} \bar{u} \frac{\partial \bar{u}}{\partial x} + \bar{\rho} \bar{v} \frac{\partial \bar{u}}{\partial y} = \rho_{\infty} V_{\infty} \frac{dV_{\infty}}{dx} + \frac{\partial \tau}{\partial y} \quad (2)$$

y-momentum

$$\frac{\partial \bar{p}}{\partial y} = -\frac{\partial}{\partial y}(\bar{\rho} v' v') \ll \left| \frac{\partial \bar{p}}{\partial x} \right| \quad (3)$$

Energy

$$\bar{\rho} \bar{u} \frac{\partial \bar{h}}{\partial x} + \bar{\rho} \bar{v} \frac{\partial \bar{h}}{\partial y} = \bar{u} \frac{\partial \bar{p}}{\partial x} + \frac{\partial q''}{\partial y} + \tau \frac{\partial \bar{u}}{\partial y} \quad (4)$$

where h is specific enthalpy and

$$\tau = \bar{\mu} \frac{\partial \bar{u}}{\partial y} - \overline{\rho u' v'} \quad (5)$$

and

$$q'' = \bar{k} \frac{\partial \bar{T}}{\partial y} - \overline{\rho v' h'} \quad (6)$$

Considering equation (3), the pressure variation in the y -direction is neglected when compared to that of the x -direction. The term $\overline{\rho u' v'}$ in equation (5) is the so-called Reynolds' stress and is significant because it adds another unknown to the system of equations. The use of the eddy transport definitions are one method to account for this "closure" problem in turbulent boundary layers. These definitions are based on a conceptual model that ties the transport of mass, momentum and heat in a turbulent boundary layer to the motion of eddies [19]. The eddy transport equations are [32,49]

Momentum

$$-\overline{\rho u' v'} = \mu_t \frac{\partial \bar{u}}{\partial y} \quad (7)$$

Energy

$$-\overline{\rho v' h'} = c_p k_t \frac{\partial \bar{T}}{\partial y} \quad (8)$$

Substituting equations (7) and (8) into (2) and (4), and assuming constant specific heat yields [32,49]

Momentum

$$\bar{\rho} \bar{u} \frac{\partial \bar{u}}{\partial x} + \bar{\rho} \bar{v} \frac{\partial \bar{u}}{\partial y} = -\frac{d\bar{p}}{dx} + \frac{\partial}{\partial y} \left[(\mu + \mu_t) \frac{\partial \bar{u}}{\partial y} \right] \quad (9)$$

where

$$\frac{d\bar{p}}{dx} \approx -\rho_\infty V_\infty \frac{dV_\infty}{dx} \quad (10)$$

since the slight pressure gradient in the y -direction can be ignored for this development;

Energy

$$c_p \left(\bar{\rho} \bar{u} \frac{\partial \bar{T}}{\partial x} + \bar{\rho} \bar{v} \frac{\partial \bar{T}}{\partial y} \right) = \bar{u} \frac{d\bar{p}}{dx} + \frac{\partial}{\partial y} \left[\left(k + \frac{c_p \mu_t}{Pr_t} \right) \frac{\partial \bar{T}}{\partial y} \right] + (\mu + \mu_t) \left(\frac{\partial \bar{u}}{\partial y} \right)^2 \quad (11)$$

Equations (9) and (11) can be nondimensionalized using the following equations (assuming constant properties) [49]

$$x^* = \frac{x}{\delta_t} \quad (12)$$

$$y^* = \frac{y}{\delta_t} \quad (13)$$

$$\bar{u}^* = \frac{\bar{u}}{V_\infty} \quad (14)$$

$$\bar{\rho} \bar{v}^* = \frac{\bar{\rho} \bar{v}}{\rho_\infty V_\infty} \quad (15)$$

$$\bar{T}^* = \frac{\bar{T} - T_{aw}}{T_w - T_{aw}} \quad (16)$$

$$\bar{p}^* = \frac{\bar{p} - p_\infty}{\rho_\infty V_\infty^2} \quad (17)$$

$$\bar{\rho}^* = \frac{\bar{\rho}}{\rho_\infty} \quad (18)$$

where δ_t is the turbulent velocity boundary layer thickness and is the characteristic length of choice considering its importance when comparing the present work to the literature (see Section 3.3.1).

When equations (12-18) are substituted into equations (1), (9) and (11), the resulting equations become

Continuity

$$\frac{\partial}{\partial x^*} (\bar{\rho}^* \bar{u}^*) + \frac{\partial}{\partial y^*} (\bar{\rho} \bar{v}^*) = 0 \quad (19)$$

Momentum

$$\bar{\rho}^* \bar{u}^* \frac{\partial \bar{u}^*}{\partial x^*} + \bar{\rho} \bar{v}^* \frac{\partial \bar{u}^*}{\partial y^*} = -\frac{d\bar{p}^*}{dx^*} + \frac{1}{Re} \frac{\partial}{\partial y^*} \left[\left(1 + \frac{\mu_t}{\mu} \right) \frac{\partial \bar{u}^*}{\partial y^*} \right] \quad (20)$$

Energy

$$\frac{1}{Ec} \left(\bar{\rho}^* \bar{u}^* \frac{\partial \bar{T}^*}{\partial x^*} + \bar{\rho} \bar{v}^* \frac{\partial \bar{T}^*}{\partial y^*} \right) = \bar{u}^* \frac{\partial \bar{p}^*}{\partial x^*} + \frac{1}{Ec} \frac{1}{Re} \frac{\partial}{\partial y^*} \left[\left(\frac{1}{Pr} + \frac{1}{Pr_t} \frac{\mu_t}{\mu} \right) \frac{\partial \bar{T}^*}{\partial y^*} \right] + \frac{1}{Re} \left(1 + \frac{\mu_t}{\mu} \right) \left(\frac{\partial \bar{u}^*}{\partial y^*} \right)^2 \quad (21)$$

where the turbulent Prandtl number is

$$Pr_t = \frac{\mu_t c_p}{k_t} \quad (22)$$

Upon closer inspection, equations (19-21) are in the same form as equations (1), (9) and (11), respectively, but with the addition of several nondimensional parameters. This is significant because the governing equations are of the same form and the nondimensional parameters can be readily computed and tracked throughout testing. These nondimensional parameters are examined more closely in the following section.

2.2 Nondimensional Parameters

This section will define and discuss the nondimensional parameters shown in the previous section, as well as those typically used to report heat transfer data.

2.2.1 Reynolds Number, Re

The Reynolds number is the primary parameter which correlates the viscous nature of all newtonian fluids and is defined as [48]

$$Re_x = \frac{\rho V x}{\mu} \quad (23)$$

where x is the distance from some reference location and the flow properties are evaluated at the same location. The choice of distance is arbitrary; the Reynolds number is based on a characteristic length, be it hydraulic diameter or boundary layer thickness and must be chosen to correspond to the location of interest. The Reynolds number can also be thought of as the ratio of inertial forces to viscous forces.

2.2.2 Eckert Number, Ec

This nondimensional parameter compares the specific kinetic energy of the flow and the specific enthalpy difference in the boundary layer [19], and is defined as [49]

$$Ec = \frac{V_\infty^2}{c_p(T_w - T_{aw})} \quad (24)$$

where the adiabatic wall temperature, T_{aw} , is [21]

$$T_{aw} = T_\infty + r \frac{V_\infty^2}{2c_p} = T_\infty \left[1 + \frac{r(\gamma - 1)}{2} M_\infty^2 \right] \quad (25)$$

for a calorically perfect gas. The recovery factor, r , is found in high speed flow calculations to account for compressibility effects and is generally taken to be $Pr^{\frac{1}{3}}$ [21].

2.2.3 Mach Number, M

The Mach number is defined as [5]

$$M = \frac{V}{a} \quad (26)$$

where a and V are the speed of sound and magnitude of velocity, respectively, at the point of interest. The Mach number, although not explicitly shown in equations (19-21), is found imbedded in equation (24) through T_{aw} . Thus, the Mach number is an important parameter associated with high speed flows.

2.2.4 Prandtl Number, Pr

The Prandtl number is defined as follows [19]

$$Pr = \frac{\mu c_p}{k} = \frac{\nu}{\alpha} \quad (27)$$

where α is the thermal diffusivity

$$\alpha = \frac{k}{\rho c_p} \quad (28)$$

and ν is the kinetic viscosity

$$\nu = \frac{\mu}{\rho} \quad (29)$$

Therefore, the Prandtl number indicates the relative strength of energy transfer due to inertia and diffusion.

2.2.5 Stanton Number, St

The Stanton number is one way to present heat transfer data and is typically used for internal flows that are not fully developed, i.e. the upper and lower boundary layers have not merged. The

Stanton number is defined as [19]

$$St = \frac{h}{\rho_{\infty} V_{\infty} c_p} \quad (30)$$

where h is the heat transfer coefficient. The Stanton number is imbedded in the nondimensionalized equations upon closer examination of the second term on the right hand side of equation (21). Expanding this term and combining equations (23) and (27) with characteristic length, L , yields

$$\frac{1}{Ec} \frac{\partial}{\partial y^*} \left(\frac{\mu}{\rho V L} \frac{k}{\mu c_p} \frac{\partial T^*}{\partial y^*} + \frac{\mu}{\rho V L} \frac{k_t}{\mu_t c_p} \frac{\mu_t}{\mu} \frac{\partial T^*}{\partial y^*} \right). \quad (31)$$

Consider a control volume enclosing the cavity insert surface, as shown in Figure 1. An energy

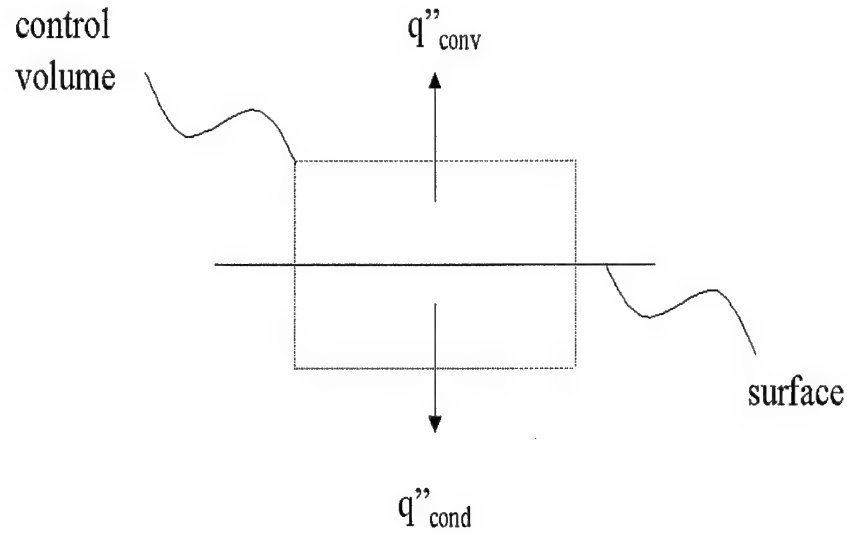


Figure 1. Control volume around cavity surface

balance on the control volume yields

$$q''_{conv} = -q''_{cond} \quad (32)$$

or, using Fourier's Law for one dimensional heat flux and Newton's Law of Cooling at the wall [19]

$$h(T_w - T_{aw}) = - \left[-k \left(\frac{\partial T}{\partial y} \right)_{y=0} \right] = k \frac{(T_w - T_{aw})}{L} \left(\frac{\partial \bar{T}^*}{\partial y^*} \right)_{y=0} \quad (33)$$

using equation (16) and equation (13) nondimensionalized with the characteristic length, L . Substituting this result into the first term of equation (31) yields

$$\frac{\mu}{\rho V L} \frac{k}{\mu c_p} \frac{\partial \bar{T}^*}{\partial y^*} = \frac{h}{\rho V c_p} = St \quad (34)$$

Thus, the Stanton number is a measure of the heat transfer at the interface between the bulk motion of the fluid and the solid surface.

2.2.6 Grashof Number, Gr

The Grashof number for uniform wall temperature is defined as [8]

$$Gr_L = \frac{g \beta L^3 \Delta T}{\nu^2} \quad (35)$$

where β is the volumetric thermal expansion, defined as [19]

$$\beta = -\frac{1}{\rho} \left(\frac{\partial \rho}{\partial T} \right)_p = \frac{1}{T} \quad \text{for an ideal gas} \quad (36)$$

The Grashof number is the ratio of buoyancy forces to viscous forces acting on a fluid element [19] and plays a key role in determining the importance of free convection effects. For instance, if $Gr_L/Re_L^2 \ll 1$, then the forced convection effects are dominant and the free convection effects can be neglected. The opposite is true for $Gr_L/Re_L^2 \gg 1$. For $Gr_L/Re_L^2 \sim 1$, both free and forced convection effects must be considered. The Grashof number is not shown in the nondimensional

equations because body forces (e.g. gravity) were assumed negligible. This assumption is verified below.

The relative effects of forced and free convection were determined to assess the validity of negligible body (gravity) forces. The need to determine the relative effects of forced and free convection was driven by the flow in the cavity. A recirculation zone in the cavity was known to exist which could cause an increase or decrease in heat transfer effects based on the directions of the flow and gravity field directions. The solution was obtained without gravity effects to determine if a second solution incorporating gravity effects would be required. Considering that the inclined trailing wall is the region of interest, the Grashof and Reynolds numbers were calculated along this surface. These numbers were calculated at both extremes of the inclined trailing wall with distances measured from the reattachment point. Using equations (23) and (35) with fluid properties taken from the computational results, $Gr_L/Re_L^2 = 5E - 4$ at the top of the incline and $Gr_L/Re_L^2 = 3E - 4$ at the bottom of inclined trailing wall. Considering the small change in surface temperature during each tunnel run, as shown in Figure 15, equation (35) could be used for uniform wall temperature. Thus, free convection effects were neglected.

Chapter 3 - Experimental Facilities

This chapter discusses the experimental facilities used to perform this research. Section 3.1 contains a discussion of the wind tunnel layout and associated hardware. Section 3.2 contains information on the data acquisition equipment, as well as the flow field visualization (schlieren) equipment. Section 3.3 contains information about the design and assembly of the cavity, as well as hardware specifically associated with the cavity. The steps taken to conduct the tests are contained in Section 3.4. Finally, Section 3.5 contains the data reduction method used to analyze the recorded temperature data.

3.1 Wind Tunnel Facilities

The present work was completed in AFIT's Mach 2.9 wind tunnel. The run time of the facility was approximately 25 seconds with approximately 7 minutes required to re-establish the operational state of 133 Pa in the evacuated chamber. The wind tunnel consisted of a plenum chamber, converging-diverging half nozzle, test section, diffuser and evacuated chamber (see Figure 2).

3.1.1 Plenum Chamber

The plenum total pressure was monitored using an ENDEVCO Model 8510C-100, 0.34 MPa (0 – 50 $psig \pm 0.5\%$) gage pressure transducer connected to an ENDEVCO Model 4428A Conditioner. Atmospheric pressure was measured using a Druck Model DPI 141 digital barometer (accuracy: 0.02% of reading plus 11.5 Pa). The plenum total temperature was monitored using a type K thermocouple connected to an Omega DP41-TC High Performance Temperature Indicator. The thermocouple/indicator combination was accurate to $\pm 1.3\text{ }^{\circ}C$ [38]. These total properties were measured downstream of the flow straightener and upstream of the nozzle throat (see Figure 3).

3.1.2 Mach 2.9 Nozzle

The flow from the plenum was accelerated by a converging-diverging half nozzle. The distance from the throat to the nozzle exit is 27 cm with an exit cross-section of 6.35 cm x 6.35 cm. The exit Mach number is $2.85 \pm 1.8\%$ with a freestream turbulence level of 0.8%, as measured by Huffman [18].

Figure 2 shows a schematic of the wind tunnel, including the plenum chamber, half-nozzle, test section and diffuser. The ceiling and sidewalls of the test section contained a section of optical glass to allow visual access to the cavity. A close-up of the half nozzle, cavity, optical sidewall

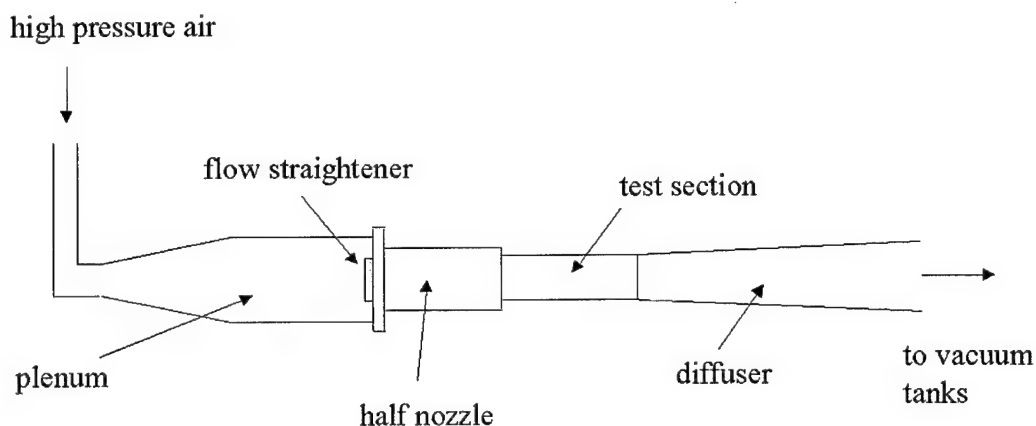


Figure 2. Schematic of AFIT's Mach 2.9 wind tunnel

and diffuser are shown in Figure 3. The cavity, insert and sidewalls are discussed in more detail in Section 3.3.

3.2 Measurement Equipment

Measurement equipment was used to not only acquire quantitative data, but also to observe the qualitative flow structure in and around the cavity.

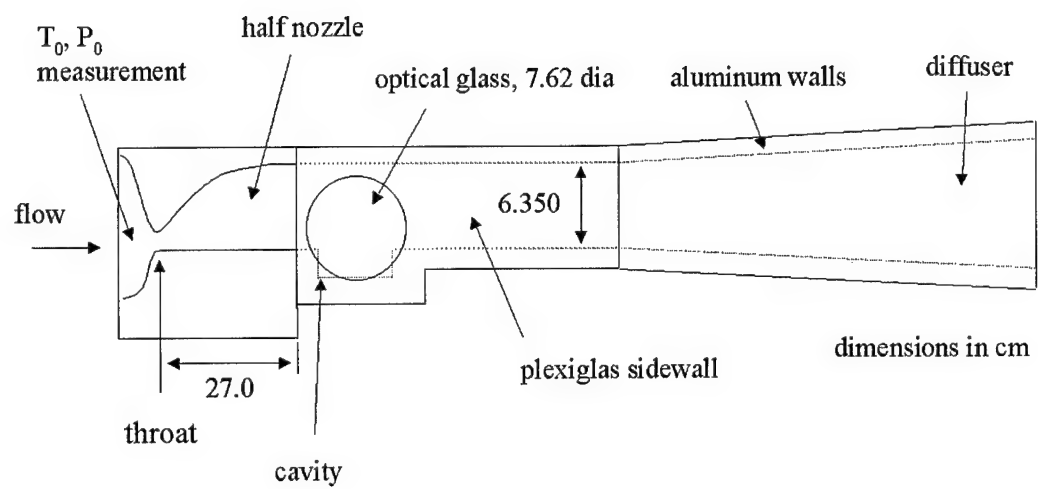


Figure 3. Schematic of half nozzle and test section

3.2.1 Data Acquisition

The data acquisition system consisted of a PC, A/D system and thirteen thermocouples. The PC was a Dell XPS R400, while the A/D system included the instruNet Model 200 Controller and Model 100 Network Device. The controller, through its accompanying software, was used to set such parameters as sampling rate and integration time, while the network device provided connection of eight thermocouples per test. The sampling rate was 7.8 Hz , with 250 points recorded per test. The accuracy of the A/D and thermocouple arrangement is $\pm 1.3\text{ C}$ [20, 38]. The thermocouples used in the cavity insert to measure surface temperature were wired single-ended to the controller to reduce ground noise. An integration time of 16 ms was used to further reduce noise. The calibration of these thermocouples is discussed in Section 3.3.3.

3.2.2 Flow Visualization

The schlieren system used for flow visualization consisted of two concave ($d = 15.24\text{ cm}$) mirrors, a mercury light source, Nikon 90S camera with Kodak DCS 420 system, horizontal knife edge and a sheet of white paper. The white paper was used as a nonreflective surface that allowed the image to be captured by the digital camera. A schematic of the schlieren setup is shown in Figure 4.

As light passes through the test section, air density gradients deflect the light rays. A horizontal knife edge produces $\partial\rho/\partial y$ information, where y is defined positive vertically originating from the tunnel floor. Light regions are indicative of a positive density gradient, while dark regions are indicative of a negative density gradient [22]. This is best shown by examining the tunnel floor and ceiling. The density along the tunnel floor removed from the cavity increases in the positive y -direction due to viscous heating along the floor, as shown by the ideal gas law, $\rho = p/RT$, where R is the gas constant for air. Therefore, the schlieren image should contain a light colored bound-

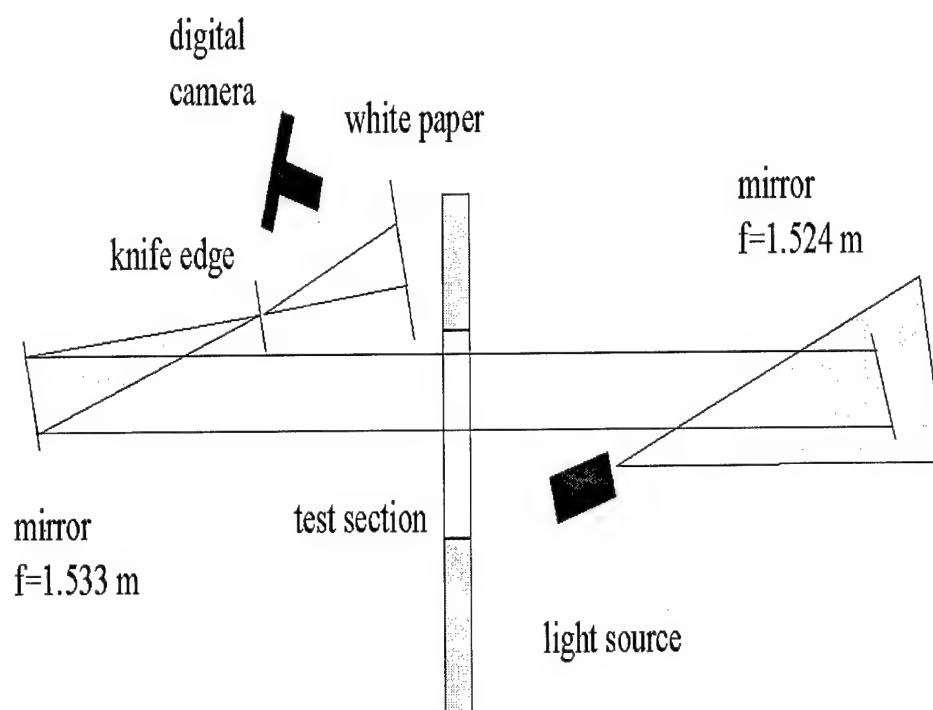


Figure 4. Schematic of schlieren setup

ary layer along the tunnel floor. The tunnel ceiling, on the other hand, should contain a dark colored boundary layer since the ceiling has an increasing density gradient in the negative y -direction, hence, a negative density gradient. Additionally, a left running oblique shock should also appear dark colored based on the direction of $\partial\rho/\partial y$, as illustrated in Figure 5.

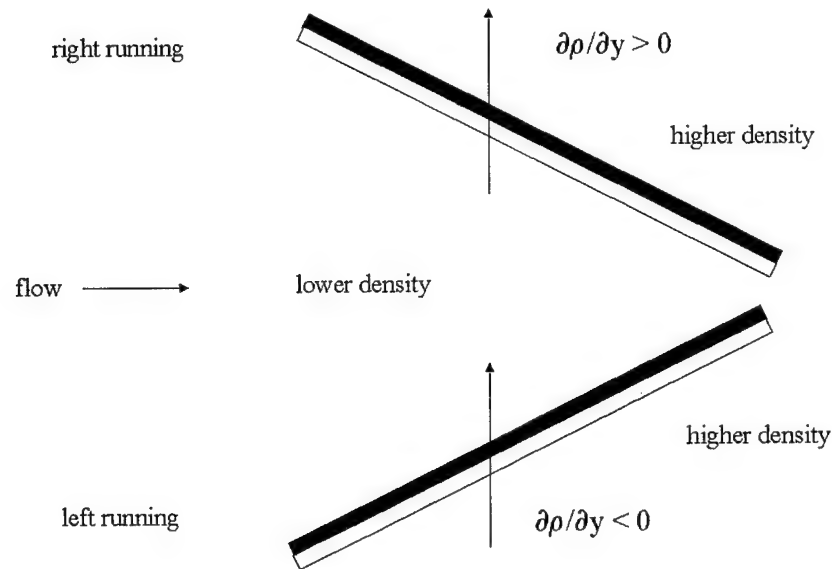


Figure 5. Schematic showing density gradient across oblique shock

The light colored region downstream of the left running wave is an area of non-equilibrium flow. The converse is true for right running waves.

3.3 Cavity Geometry

The wind tunnel test section had to be modified to incorporate a cavity to perform the present work; prior to this work, the tunnel floor did not contain a cavity. The nondimensional parameters from Section 2.2 were compared to the literature to ensure that the present work was relevant. This section contains the design, assembly process and equipment associated with the cavity.

3.3.1 Cavity Design

To faithfully reproduce the scramjet conditions, the parameters shown in Table 1 had to be matched.

Table 1. Matched parameter comparison

Parameter	Scramjet [44]	Scramjet model [10]	Related references	AFIT
M	2 – 3.7	1.9	2.92 [33]	2.9
$Re (m^{-1})$	$1.9E7 - 5.9E6$	$8.47E6$	$6.7E7$ [33]	$1.9E7$
geometry	2-D, 3-D [15]	2-D, 3-D	2-D [33]	2-D
$\delta_t (mm)$ at cavity LE	12.7 [15]	1.3	4.6 [30]	1.4
δ_t -to-depth	0.82 [15]	0.13	0.177 [30]	0.181
$T_0 (K)$	870 – 2600	830	258 [33]	295
$p_0 (kPa)$	610 – 3000	287	690 [33]	287
depth-to-pre-incline length	0.26 [15]	0.25	0.41 [33]	0.41
trailing wall angle	20° [15]	30°	20° [33]	20°

The scramjet values correspond to accelerating flight at $M_\infty = 4-8$, with the cruise condition present at $M_\infty = 8$. Davis and Bowersox [10] is specifically referenced because Davis is currently conducting research for the HyTech project.

The following is a discussion of the parameters shown in Table 1, their usefulness in designing the cavity and comparisons between the categories shown. The AFIT Mach number used was slightly higher than that of the scramjet model (values correspond to $M_\infty = 4$) and was fixed due to the half nozzle. However, the AFIT Mach number fell within the range of the operational scramjet and was, therefore, a representative Mach number. The Reynolds number was used to determine the absolute depth of the cavity based on proximity to the nozzle exit (see Section 3.3). The Reynolds number for the AFIT design fell within the range for the scramjet. In examining the Mach number and Reynolds number for the AFIT design, one will notice that they correspond to different flight Mach numbers for the operational case. This difference is due to a change in fluid properties from increased temperature and pressure for the operational scramjet. Nevertheless, the AFIT design Mach and Reynolds numbers fell within the ranges for the operational scramjet and, as

such, are representative of the flow. The flowfield was approximated as two dimensional because the cavity spanned the entire width of the tunnel. At the centerline of the scramjet, the flow is two dimensional. However, the scramjet and model were also analyzed as three dimensional to incorporate sidewall effects since the scramjet cavity width is less than the width of the combustor. This was done to allow for design and testing flexibility [15]. The AFIT turbulent boundary layer thickness at the cavity LE was on the same order as both the reference and the scramjet model. Matching this parameter was significant as it dictated the position of the cavity LE relative to the nozzle exit. The δ_t -to-depth ratio was an important parameter for comparison, together with the depth-to-length ratio, as it dictated the recirculating flow field within the cavity in terms of fixing the reattachment point on the inclined trailing wall. The boundary layer thickness and δ_t -to-depth ratio could not be matched to the scramjet because of the position of the scramjet cavity within the combustor. Boundary layer growth is enhanced in the scramjet due to the cavity being roughly centered axially within the engine. The stagnation temperature was not matched to the scramjet case, but was to the reference case due to the use of a cold flow test facility. This simplified the test by eliminating the need for tunnel wall cooling. The stagnation pressure for the AFIT design was limited by the test facilities. However, the stagnation pressure did match the scramjet model and was on the same order as that used in the scramjet and related reference. Matching the depth-to-pre-incline length ratio was important to reproduce the flowfield within the cavity. Increasing this ratio for a given depth causes less of the free shear layer to enter the cavity. Thus, with the cavity flow field not established in the same manner as the scramjet case, the heat transfer to the inclined trailing wall could be different by not presenting a stagnation region. Therefore, the depth-to-pre-incline length ratio for the AFIT design was on the same order as the other designs and models referenced. The inclination angle for the trailing wall was a significant parameter since it would

dictate the relative effect of stagnation at the trailing wall. The AFIT design matched both the scramjet and the related reference.

Although not shown in Table 1, two other parameters described in Section 2.2 require discussion here. The Prandtl and Eckert numbers were not well matched due to the use of cold flow. As discussed earlier, cold flow experiments are still a useful precursor to hot flow experiments. However, in a hot flow experiment, the Eckert and Prandtl numbers would likely be lower due to the increase in fluid temperature and the presence of fuel, but would depend on the fluid velocity and specific heat.

The distance from the nozzle exit to the leading edge of the cavity was a primary area of the cavity design since this determined the boundary layer thickness at the cavity LE. The present cavity geometry resembles the geometry of research found in the open literature. Davis and Bowersox [10] examined the flow structure in and around a cavity of nearly the same geometry as the present work, though their work did not include heat transfer calculations. Roshko and Thomke [30], Horstman *et al.* [17] and Settles *et al.* [33] examined similar cavity flow geometries. Horstman *et al.* [17] and Settles *et al.* [33] examined the reattachment of a free shear layer that traversed an open cavity with a 20° inclined trailing wall. (Horstman *et al.* [17] performed a computational study and comparison based on the experimental results of Settles *et al.* [33]). Roshko and Thomke [30] examined the reattachment of a free shear layer from a rear facing step with no trailing wall, i.e. a trailing flat plate. The boundary layer thickness, Reynolds number and Mach number reported in these articles formed the basis of comparison. All of the work discussed above were performed at or about $M = 2.9$, the same as in the current study.

The boundary layer thickness at the cavity leading edge was calculated using turbulent, compressible boundary layer theory. Van Driest [42] suggests that the compressible boundary layer thickness can be estimated from incompressible boundary layer theory using an adjusted Reynolds

number at the wall based on a power law approximation of Sutherland's viscosity law [32]

$$\frac{\mu_w}{\mu_\infty} = \left(\frac{T_w}{T_\infty} \right)^\omega \quad (37)$$

and the ideal gas law evaluated at the wall and referenced to the freestream, namely

$$\rho_w = \rho_\infty \left(\frac{T_w}{T_\infty} \right) \quad (38)$$

since effect of the pressure gradient, $\partial p / \partial y$, through the boundary layer is negligible, as discussed in Section 2.1. When equations (37) and (38) are combined with equation (23), the adjusted Reynolds number at the wall becomes

$$Re_w = x Re \left(\frac{T_w}{T_\infty} \right)^{-(1+\omega)} \quad (39)$$

For the AFIT Mach 2.9 wind tunnel, the freestream Reynolds number was measured by Latin [22] to be $Re = 1.9E7 \text{ m}^{-1}$ for $T_0 = 293 \text{ K}$, and $T_{aw} = 275 \text{ K}$. Schlichting [32] and Van Driest [42] both use $\omega = 0.76$ as a reasonable power-law approximation to Sutherland's viscosity law. This law was developed to determine the viscosity at the wall based on a reference condition (in this case, the freestream condition). The Reynolds number calculation was useful here because it accounted for changing air density and viscosity at the wall due to viscous heating. The result is $Re_w = 1.2E5$ and will be used in equation (42).

The compressible turbulent boundary layer thickness at position, x , from the nozzle exit to the cavity leading edge was calculated from equations (40-42) [42]

$$\delta_t = \frac{x C_f}{2} \frac{0.558}{\sqrt{C_f} \left(1 - \frac{2\sqrt{C_f}}{0.558} \right)} \quad (40)$$

where

$$c_f = \frac{0.558C_f}{(0.558 + \sqrt{C_f})} \quad (41)$$

and

$$C_f = \left[\frac{0.242}{\log_{10}(Re_w C_f)} \right]^2 \quad (42)$$

The distance, x from the nozzle exit to the cavity LE in equations (39) and (40), was determined based on the following process. First, the open literature was reviewed to determine relevant ranges of $depth/\delta_t$ and $width/depth$. Members of the HyTech program were also consulted. This review yielded $1.38 < depth/\delta_t < 9.25$ and $5.99 < width/depth < 20$ [30, 31, 33]. The $depth/\delta_t$ ratio was important, as discussed above, while $width/depth$ was important to maintain two dimensional flow in the cavity. As such, $width/depth$ was chosen to be 10, thus fixing the depth based on existing tunnel geometry. Finally, the distance, x , was varied until $depth/\delta_t$ and Re_x fell within the ranges specified. The end result was to place the cavity leading edge 4.0 cm from the nozzle exit, yielding a $width/depth = 8.1$. This ratio was on the same order as the experiment of Horstman *et al.* [17] (see comparison in Table 2).

Table 2. Cavity geometry comparison

Parameter	present work	Roshko and Thomke [30]	Horstman <i>et al.</i> [17]
δ_t (mm)	1.42	4.60	3.28
$depth/\delta_t$	5.53	5.53	7.74
$width/depth$	8.14	axisymmetric body of revolution	5.99
pre-incline flow length-to-depth	2.44	rear facing step only	2.44

The boundary layer thickness calculation was also compared to measurements and calculations performed by Latin [22]. Latin performed turbulent boundary layer measurements on flow through the AFIT $M = 2.9$ tunnel using a Pitot probe and schlieren flow visualization, as well as calculations using an integral analysis of the Navier-Stokes' equations. Latin's data were taken or

calculated at 53.975 *cm* from the nozzle exit. The Pitot probe measurements and integral analysis yielded a boundary layer thickness of 12.4 *mm*, while the schlieren photographs yielded a boundary layer thickness of 13.8 *mm*. When equations (40-42) described above were applied at the same tunnel location as that used in Latin's research, the boundary layer thickness was calculated to be 13.3 *mm*, a difference of 7% from the Pitot probe measurements and integral analysis and a difference of 3.6% from the schlieren photographs. These comparisons indicate that the analytical approach shown in equations (40-42) was accurate, and that the boundary layer experienced very little growth upstream of the nozzle exit. Therefore, the boundary layer thickness calculated at the rear-facing step of the cavity using equations (40-42) was reasonable and any boundary layer growth upstream of the nozzle exit was negligible.

The modified floor section, plexiglas inserts and sidewalls were manufactured by the AFIT Machine Shop. Referring to Figure 3, the sidewalls were constructed of plexiglas for optical accessibility and to ensure thermal and electrical isolation. The optical glass insert was placed such that a large portion of the cavity flowfield could be captured by the flow visualization technique.

The forward portion of the cavity was designed to be recessed in the floor cavity, minimizing surface discontinuities upstream of the cavity. The rear portion of the cavity insert was designed to be flush with the tunnel floor, thus approximating the continuous surface of the actual hardware. In doing so, the shock could be analyzed downstream of the cavity insert. This information could prove useful in future attempts to determine the best trailing wall geometry in terms of thermal management.

Eleven thermocouples, labeled according to Table 3, were placed at various points of interest in the inclined trailing wall cavity. These positions were on the cavity floor, just prior to the incline; at the beginning of the incline, across the middle of the incline, at the top of the incline, and downstream of the incline.

Table 3. Thermocouple station labels

Description	Axial distance (cm) from Figure 6	Station
Bottom	1.800	1
1 st position on incline	2.200	2
2 nd position on incline	2.533	3
3 rd position on incline	2.866	4
Center	3.200	5
2 nd from top	3.500	6
Top of incline	3.800	7
Top	4.75	8
Left	3.200	9
Right	3.200	10
Lower temperature	0.25	11

Three thermocouples across the middle of the cavity insert were used to verify the two dimensional flow assumption. Figure 6 shows a schematic of the thermocouple positions within the cavity insert.

The thickness of the cavity insert was determined by comparing projected convective and conductive heat transfer rates. Radiation from the plexiglas was assumed to be negligible. This assumption is verified in Section 5.1.1. Furthermore, the air in the tunnel was considered to be a non-participating medium; scattering effects were not appreciable since the air was virtually free of particulate matter and emission and absorption effects were low, considering the air temperature [35]. The convective and conductive rates were compared by using Fourier's Law [19] for one dimensional, constant property heat flux

$$q_{cond}'' = -k \frac{\partial T}{\partial y} = -k \frac{\Delta T}{\Delta y} \quad (43)$$

and Newton's Law of Cooling [21] on a flux basis

$$q_{conv}'' = h\Delta T \quad (44)$$

Combining equations (43) and (44) and solving for the plexiglas thickness, Δy , yields

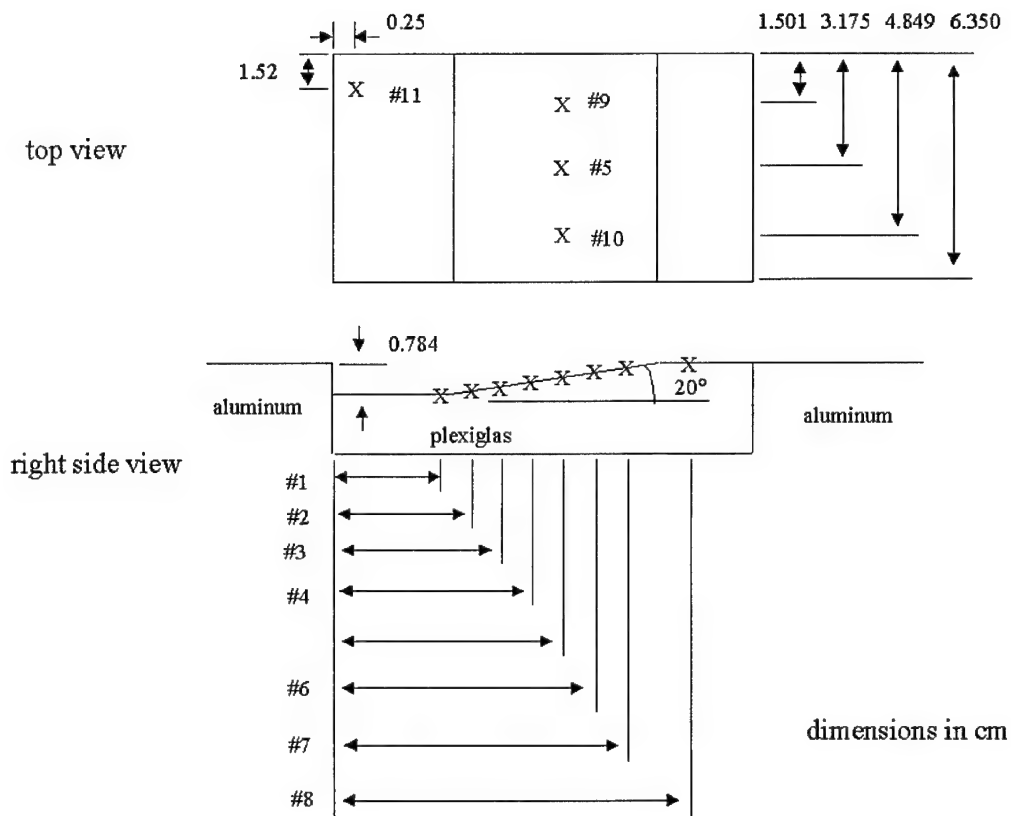


Figure 6. Placement of thermocouples in cavity insert

$$\Delta y = 20 \left[\frac{k_{plexi}(T_w - T_0)}{h(T_w - T_{aw})} \right] \quad (45)$$

where the temperature at the bottom of the cavity insert was taken to be equal to the stagnation (room) temperature. The factor of 20 was used so that the convection effects into the air stream would dominate the conduction effects through the plexiglas. This thickness of plexiglas was significant considering the assumptions inherent to the data reduction technique. This technique required that the object containing the surface of interest not only be at a uniform temperature, but also that the object can be modeled as a semi-infinite solid (see Section 3.5).

The heat transfer coefficient used in equation (45) was determined as follows. The heat transfer coefficient for a flat plate and a flat face stagnation point for the same flow conditions in the tunnel were predicted using the literature [41, 42] and [49], respectively. The flat plate heat transfer coefficient was calculated to be $200 \text{ W/m}^2\text{K}$ and the flat face stagnation point heat transfer coefficient was calculated to be $470 \text{ W/m}^2\text{K}$. These values represent the expected lower and upper bounds, respectively, of the heat transfer coefficient. The choice of heat transfer coefficient for use in equation 45 was chosen to be $220 \text{ W/m}^2\text{K}$, as it was expected to be close to the flat plate value due to the small inclination angle.

With the approximate heat transfer coefficient in hand, together with the *width/depth* ratio shown in Table 2, the final cavity insert geometry was determined, as shown in Figure 7. The cavity is shown with the inclined trailing wall cavity insert installed. A second cavity insert was built, which completely filled the cavity to simulate a flat plate. This second insert had the same dimensions of the cavity interior and was used to determine the flat plate Stanton number variation for comparison with those from the inclined trailing wall insert. The flat plate insert contained two thermocouples at stations 1 and 8 (see Table 3). Both of the cavity inserts were attached to the tunnel floor according to Figure 8.

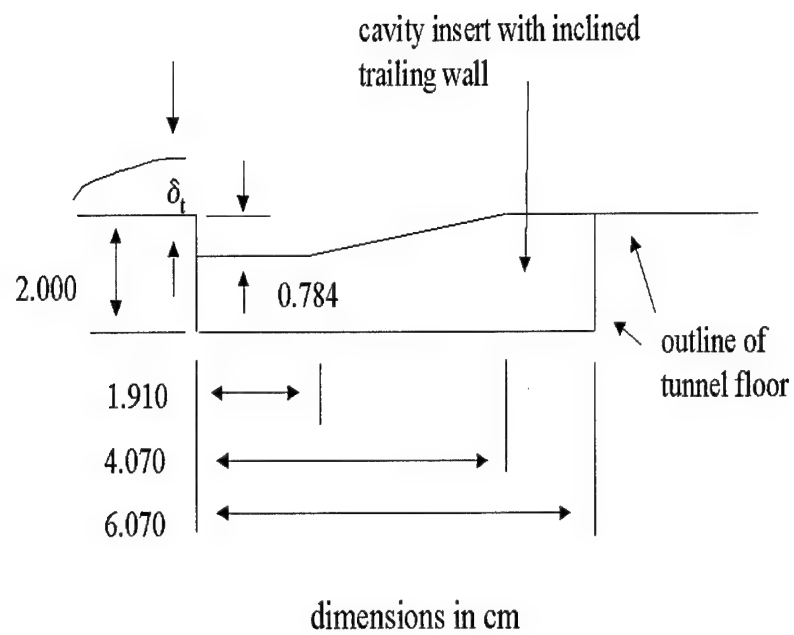


Figure 7. Final cavity geometry

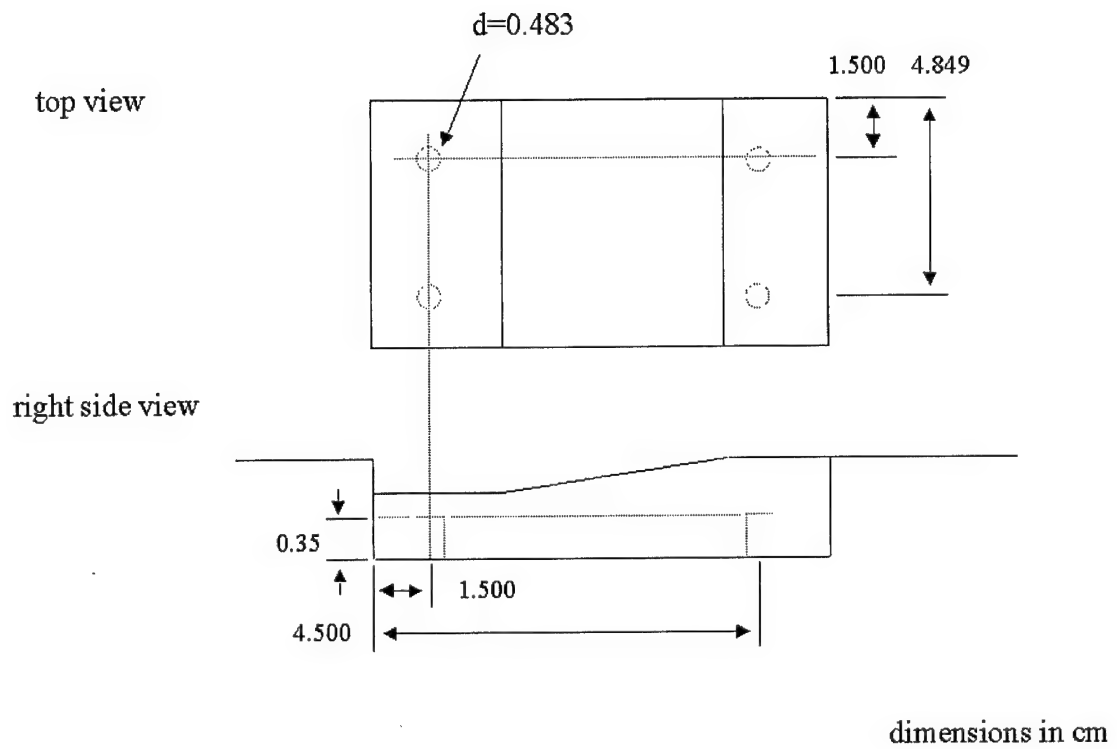


Figure 8. Placement of cavity insert attachment bolts

The attachment bolts were positioned such that the force on the cavity would be evenly distributed, while maintaining access for the thermocouples. The bolt size was recommended by a member of the AFIT Model Shop based on the projected force on the insert. This force was determined by considering that the bottom of the insert would be exposed to atmospheric pressure through the bolt holes and the top surface would be exposed to the static pressure of the freestream (see Section 5.1 for value). As an increased margin of safety and to more accurately match the pressure inside the cavity, the static pressure was reduced by half for this force calculation. The resulting force that each bolt was required to support was 90 N .

3.3.2 Cavity Assembly

To ensure the position of the thermocouples at the surface, each insert was clamped together with a negative of its top surface. This is shown schematically in Figure 9. This method allows

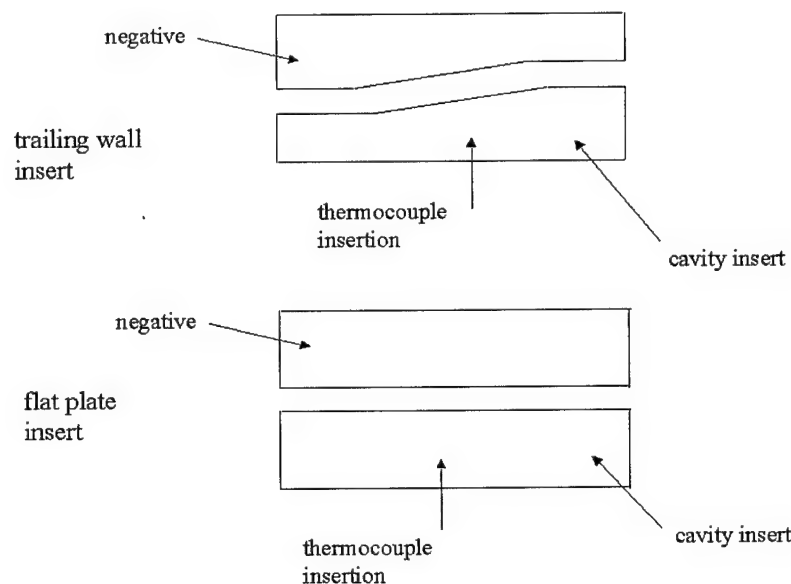


Figure 9. Schematic of cavity inserts and negatives of upper surfaces

the thermocouples to be installed from the bottom of the insert and located accurately at the insert

surface. The importance of thermocouple juxtaposition to the surface is seen in equation (51) and is discussed more in Section 3.5.

Omegabond 101 Epoxy Adhesive was used to set the thermocouples into each insert. This epoxy was chosen because of its relatively high thermal conductivity ($k = 1.04 \text{ W/mK}$) and relatively short (28 hours) full-cure time. Holes were drilled through the plexiglas at the locations shown in Table 3. The epoxy was injected into these holes ($d = 1.02 \text{ mm}$) from the bottom of the insert, using a syringe. Note that only a scant amount of epoxy was used to secure the thermocouples at the insert surface.

3.3.3 Cavity Hardware

Type T thermocouples were used to measure the surface temperature of the inclined trailing wall and flat plate cavity inserts. The thermocouple lead wires were 0.127 mm in diameter, with a bead diameter of approximately 0.254 mm . The thermocouples were calibrated at room temperature using an Omega Omni-Cal and type K thermocouple, which is accurate to $\pm 0.1 \text{ C}$, and at a lower temperature (16 C) with a NESLAB RTE-100, which is accurate to $\pm 0.1 \text{ C}$. The lower calibration temperature was chosen based on the lowest observed temperature from early tests.

In order to assess temperature uniformity through the cavity insert, the temperature at the bottom of the cavity (station 11) was monitored using a surface mount (0.076 mm thick) type K thermocouple placed between the insert and the cavity floor in the upstream, left corner, as shown in Figure 6, and an Omega DP41-TC High Performance Temperature Indicator. The accuracy of this thermocouple/indicator combination was the same as that used for monitoring the stagnation temperature.

3.4 Experimental Procedure

The cavity insert and interior tunnel walls were allowed to come to thermal equilibrium. This was verified by comparing the temperature readings of thermocouples at stations 1, 8 and 11 (see Table 3). Once these temperature readings were the same, the data acquisition system was started. The vacuum tanks downstream of the diffuser (see Figure 2) were opened to the test section to evacuate the test section and plenum chamber. The high pressure tank upstream of the plenum chamber was opened beginning the supersonic flow through the nozzle and test section. After approximately 25 *sec*, the vacuum tanks were at the same pressure as the high pressure supply, ceasing supersonic flow through the test section. The high pressure side and vacuum tanks were closed to the test section, in that order. The data acquisition system ceased recording data approximately 3 *sec* after the flow ceased.

The thermocouple used to verify insert temperature uniformity at station 11 showed only a difference of 0.6 *C* from the measured stagnation temperature and a difference of 0.4 *C* from that at stations 1 and 8 before each test. These differences were within the accuracy of their respective systems. Therefore, the tunnel walls and cavity insert were considered to be in thermal equilibrium before each run.

3.5 Data Reduction

The Stanton number was determined analytically using first principles. Consider the control volume shown in Figure 1 for the plexiglas insert. The heat transfer coefficient from equation (33) becomes

$$h = \frac{-k_{plexi} \left(\frac{\partial T}{\partial y} \right)_{y=0}}{T_w - T_{aw}} \quad (46)$$

If a periodic function for T_w is assumed, then $(\partial T / \partial y)$ at $y = 0$ can be evaluated using the classi-

cal, analytical solution for periodic temperature input at the surface [6]

$$T(y, t) = Ae^{-y(\omega/2\alpha)^{\frac{1}{2}}} \cos \left[\omega t - \left(\frac{\omega}{2\alpha} \right)^{\frac{1}{2}} y + \frac{\pi}{2} \right] + T_i \quad (47)$$

assuming that the object containing the surface of interest is at a uniform temperature at $t = 0$ and that the object is a semi-infinite solid. The phase shift, $\pi/2$, amplitude, A , and frequency, ω , are all determined by a curve fit to the thermocouple temperature data. Equation (47) can be modified to correspond to surface temperatures, as shown below

$$T_w(0, t) = A \cos \left[\omega t + \frac{\pi}{2} \right] + T_i \quad (48)$$

The experimental temperature history is well approximated by a sinusoid, as shown in Figure 10. Hence, a curve fit to the data can be used to calculate the heat transfer coefficient. This method of

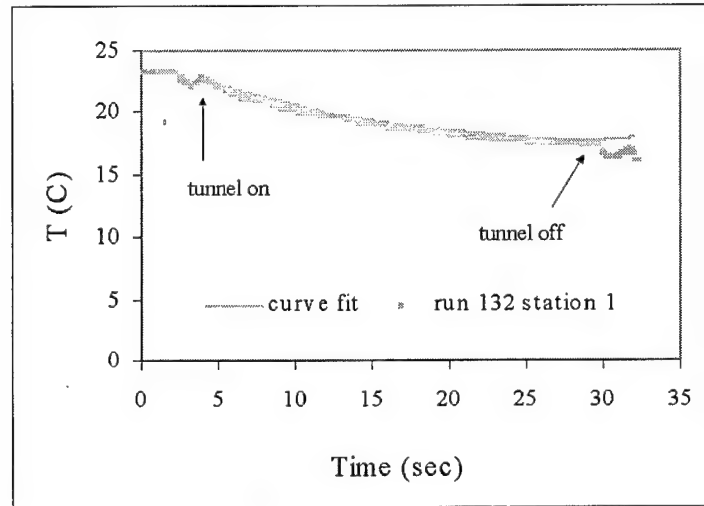


Figure 10. Comparison between fit and recorded data for flat plate; station 1

determining heat transfer data using a fit to recorded temperatures has been performed elsewhere. Abuaf *et al.* [1] performed heat transfer calculations on turbine blades (airfoils) with varying de-

degrees of surface treatment using the temperature-time histories from thermocouples. A fit to this recorded data was obtained using a lumped capacitance approximation, with subsequent heat transfer coefficient calculation obtained from the curve fit temperature history.

Following the example of Abuaf *et al.*, a curve fit to the recorded temperature data was determined with appropriate selection of the temperature amplitude, A , and frequency, ω , assuming the thermocouples were positioned at the surface, i.e. using equation (48). This selection was performed by varying A and ω until a minimum value of the root mean square, given by

$$RMS = \sqrt{\sum (T_{fit} - T_{rec})^2} \quad (49)$$

was obtained over the tunnel operating time. However, the thermocouples could not be located exactly at the surface of the insert without interrupting the flow field. Thus, the actual temperature sensing location was removed from the surface by some fraction of the bead diameter. Therefore, the temperature amplitude required correction to account for this small, but non-trivial, distance.

A series of measurements were taken at several thermocouple stations to determine the thermocouple bead placement relative to the insert surface. The average distance was measured to be 0.127 mm. As a conservative estimate, this distance was increased to include one-half of the bead diameter to better account for the actual thermocouple sensing location, yielding a distance of 0.254 mm. This distance was used to determine the corrected temperature amplitude using the curve fit temperature amplitude obtained from equation (48) in the following manner and shown schematically in Figure 11. The temperature amplitude, A , and frequency, ω , were determined by curve fit with the recorded temperature. The corrected temperature amplitude, A_{corr} , was obtained by tracing the exponential component of equation (47) back to the ordinate axis by the known distance, i.e. 0.254 mm. Only the exponential component was used because it represented the upper

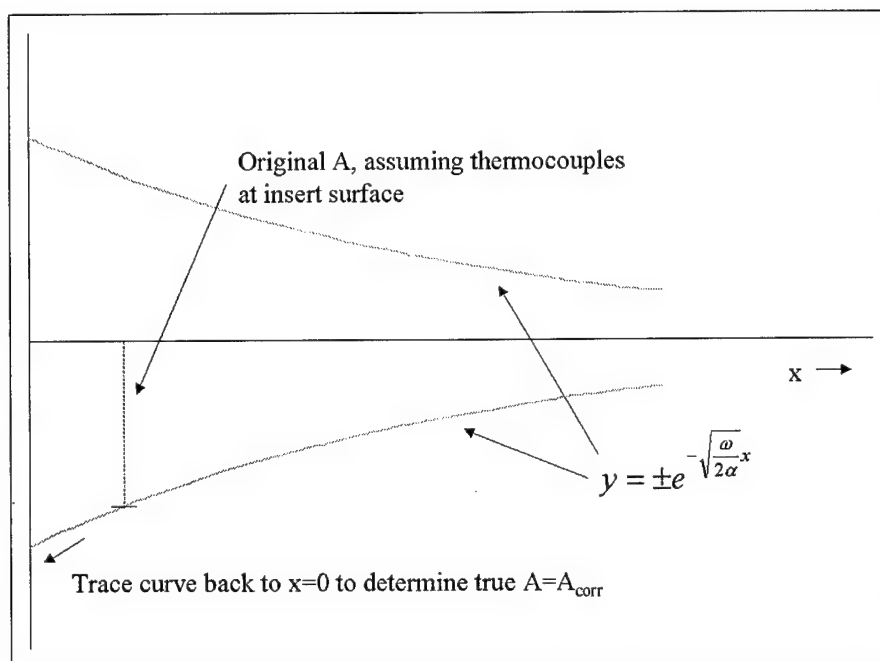


Figure 11. Determination of corrected temperature amplitude

and lower bound (amplitude) for the periodic component. The corrected temperature amplitude was the actual temperature amplitude at the surface and was determined by

$$A = A_{corr} e^{-y(\omega/2\alpha)^{\frac{1}{2}}} \quad (50)$$

where ω was the same value as that determined by the curve fit and α was evaluated using the thermophysical properties of the epoxy adhesive [38]: $\rho = 1710 \text{ kg/m}^3$, $k = 1.04 \text{ W/mK}$ and $c_p = 963 \text{ J/kgK}$. With the corrected temperature amplitude in hand, equation (48) was used to represent the surface temperature leading to the surface heat transfer coefficient. The Stanton number was determined from the heat transfer coefficient using equation (30).

The assumption that the plexiglas insert behaves as a semi-infinite solid requires further discussion here. Incropera and DeWitt [19] detail the derivation of equation (51), beginning with the one dimensional heat equation for a plane wall with no internal heat generation and a convection boundary condition, which was the case here. The conduction was assumed to be one dimensional considering the short run times and dominance of convection over conduction. The result is

$$\frac{T(y, t) - T_i}{T_{aw} - T_i} = \text{erfc} \left(\frac{y}{2\sqrt{\alpha t}} \right) - \left[\exp \left(\frac{hy}{k} + \frac{h^2 \alpha t}{k^2} \right) \right] \left[\text{erfc} \left(\frac{y}{2\sqrt{\alpha t}} + \frac{h\sqrt{\alpha t}}{k} \right) \right] \quad (51)$$

where y is the vertical distance from the surface, T_i is the initial temperature of the insert and erfc is the complimentary error function. At the surface of the insert, $y = 0$ and equation (51) is reduced to

$$\frac{T(0, t) - T_i}{T_{aw} - T_i} = 1 - \left[\exp \left(\frac{h^2 \alpha t}{k^2} \right) \right] \left[\text{erfc} \left(\frac{h\sqrt{\alpha t}}{k} \right) \right] \quad (52)$$

The solution of equation (52) using the final heat transfer coefficient along the cavity floor can

then be compared with the reading from station 11 to assess the validity of the semi-infinite solid assumption.

Chapter 4 - Computational Setup

This chapter contains a discussion about the computational facilities utilized for the present work. It also contains details about the grid generation and various inputs used in the CFD analysis as well as the CFD determination of skin friction coefficient and Stanton number.

4.1 Computational Facilities

The computational facilities included a Digital 433au Personal Workstation and the commercially available software program, FLUENT 5. This version of FLUENT included its own grid and mesh generation program, GAMBIT I, as well as the capability of analyzing supersonic and compressible flows.

The CFD results were obtained using a steady state solution. As can be seen in Figure 10, the tunnel surface temperature history is transient in nature. However, the flow structure through the tunnel reaches steady state quickly (approximately 2 – 3 *sec*). Therefore, a steady state heat transfer solution can be readily applied.

4.2 Software Inputs

This section contains information about the boundary conditions and the various settings required by FLUENT.

4.2.1 Solver Settings

The two dimensional, double precision, coupled implicit solver was chosen for the present work. The use of the coupled implicit equations was required by FLUENT to establish a supersonic, compressible flow [14]. The coupled solver solves the governing equations (Navier-Stokes equations) written in vector integral form.

Two turbulence models were employed. The standard $k - \epsilon$ model, using the familiar equations for turbulent kinetic energy and dissipation rate, were used for the flat plate case. Due to the

simplicity of the flat plate geometry, this model was an appropriate choice. The realizable $k - \varepsilon$ model was used for the cavity case due to its ability to evaluate recirculating regions. The term “realizable” is used because it models the physics of turbulent flows in a manner that is consistent with mathematical constraints on the normal stresses [14]. These constraints are determined by combining turbulent viscosity with the Boussinesq relationship for buoyancy effects in the momentum equation. The result is an altered expression for the turbulent dissipation rate from that of the standard $k - \varepsilon$ model (see Ref. [14] for resulting equation). Finally, the default constants were used for both turbulence models.

FLUENT offers two treatments for the near-wall region in its $k - \varepsilon$ models, standard and non-equilibrium wall functions. These treatments are semi-empirical relations that link the solution variables near the wall to those at the wall. Both the flat plate and cavity cases utilized the standard wall functions, requiring that the wall coordinate be in the range 30 – 60. The wall coordinate, y^+ , is defined as [21]

$$y^+ = \frac{y \sqrt{\frac{\tau}{\rho}}}{\nu} \quad (53)$$

and is a nondimensional distance from the wall in the inner boundary layer where viscous shear dominates.

A second-order upwind discretization scheme was used for the flow, turbulent kinetic energy and turbulent dissipation rate to minimize numerical or “false” diffusion. Also, under-relaxation was applied to the solid, viscosity and turbulent kinetic energy and dissipation rate to assist with convergence. Additionally, the Courant number was lowered during start-up to deter divergence.

4.2.2 Boundary Conditions

The inlet boundary conditions for the experimental test section, found in Table 4 Section 5.1, provided the initial conditions for the computational domain. The inlet boundary conditions included inputs for turbulent hydraulic diameter and turbulence intensity. These values for the AFIT $M = 2.9$ tunnel are 6.35 *cm* and 0.8%, respectively, with the turbulence intensity measured by Huffman [18]. Air was the working fluid and was modeled as an ideal gas with molecular viscosity that followed Sutherland's law of viscosity and specific heat as a function of temperature. Internal radiation exchange was neglected (this assumption is verified in Section 5.1.1).

To impose the semi-infinite solid assumption, a constant temperature boundary condition was imposed at the outer horizontal extremes of the tunnel walls, see Figure 12. An adiabatic wall condition was imposed at the outer vertical boundaries corresponding to the tunnel walls. These same boundary conditions were also imposed for the cavity domain. The thermophysical properties for plexiglas were: $k = 0.16 \text{ W/mK}$ and $c_p = 1069 \text{ J/kgK}$ [40] and $\rho = 1185 \text{ kg/m}^3$ [7].

4.3 Grid Generation

The domain space was generated using FLUENT's accompanying geometry software package, GAMBIT. The mesh for both the inclined trailing wall and flat plate cases was constructed using unstructured triangular cells. This choice was based on setup time and mesh size. One drawback of this type of cell is the possible increase in numerical diffusion since the flow cannot be aligned with a triangular grid [14]. However, in an effort to minimize this effect, the grid was adapted along all walls during the solution process to ensure that the recommended y^+ values were maintained.

Grid independence was verified by monitoring the solution residuals and the average skin friction coefficient calculation along the inclined trailing wall and along the tunnel floor for the flat

plate insert. The final solution was determined when $c_{f_{ave}}$ did not vary by more than 5% between adaptations and the residuals did not vary by more than 0.001.

Figure 12 shows a portion of the computational domain for the flat plate case, including the position of the flat plate insert used in the flat plate experiment. The cells along the interior walls

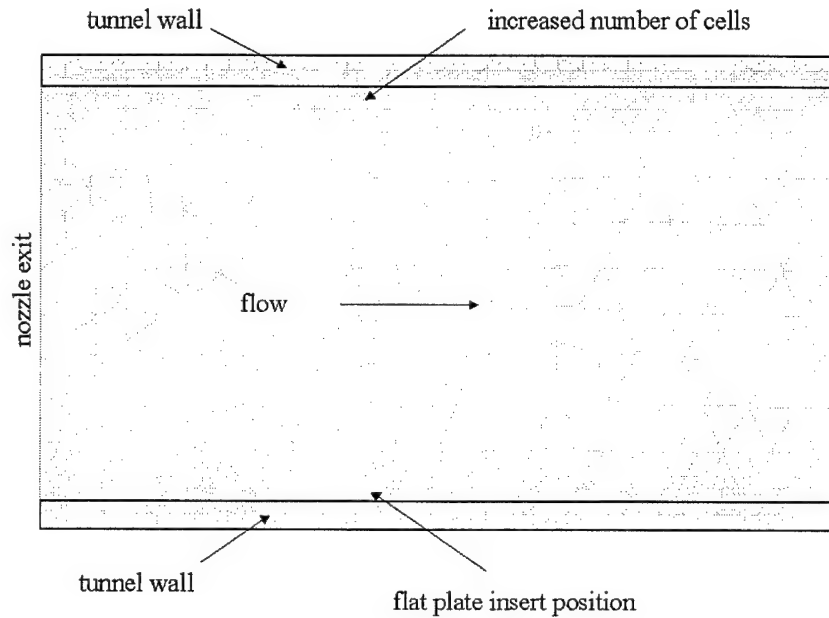


Figure 12. Forward section of grid for flat plate CFD model

were adapted to ensure the proper y^+ range with a final cell count of 17086.

The computational domain for the inclined trailing wall is shown in Figure 13. The axial limits of the flow domain are the nozzle exit and the downstream extent of the cavity, as shown in Figure 7. Figure 14 shows a closer view of the grid in the cavity.

Note the refinement along the cavity walls and in the region above the trailing wall to account for y^+ values and to capture the oblique shock, respectively. The wall cells were adapted based

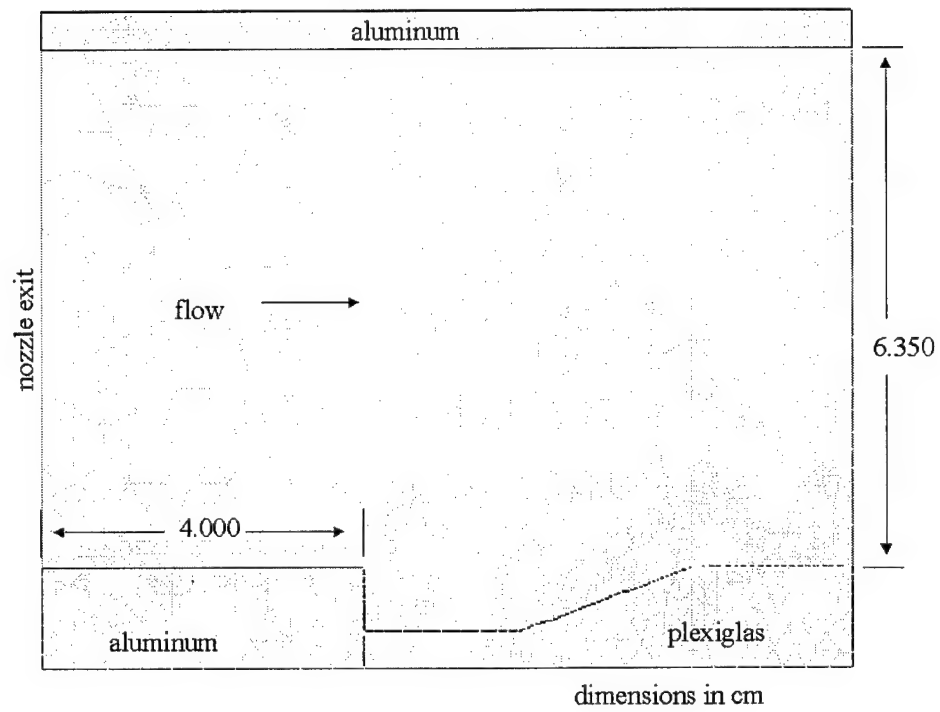


Figure 13. Grid and computational domain for cavity with inclined trailing wall

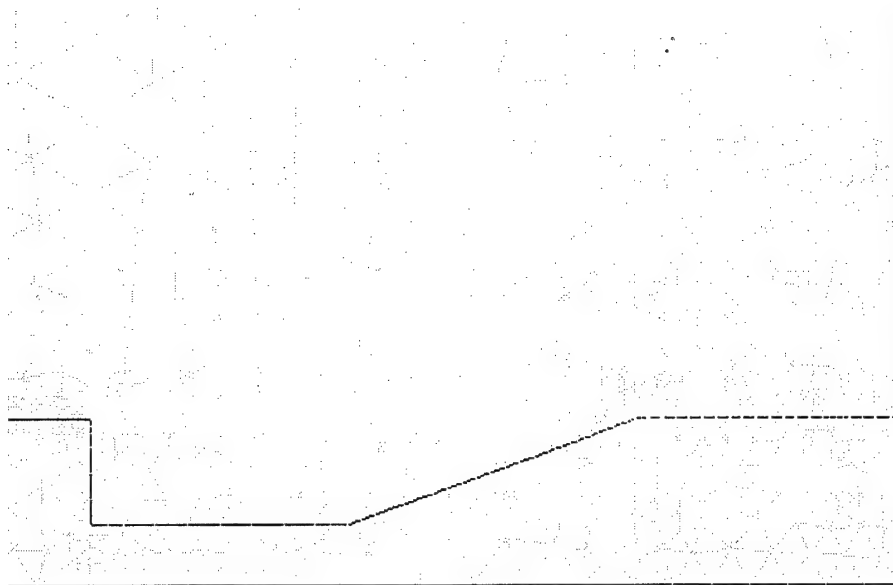


Figure 14. Closeup of cavity grid

on the recommended range for y^+ , while the area around the oblique shock was adapted based on static pressure gradient. These adaptations resulted in a final cell count of 5068.

4.4 Parameter Calculation

FLUENT determines the skin friction coefficient using equation (56) by calculating the shear stress at the wall depending on the choice of wall treatment [14]. The Stanton number is determined by equation (30). The heat transfer coefficient is calculated using an energy balance at the surface (see equation (33)). The temperature used in equation (33) is determined by the choice of wall treatment.

4.5 Code Validation

To validate FLUENT for the configuration studied, a simple test case with a known result was examined. This test case was modeled after the work performed by Latin [22] on the AFIT's Mach 2.9 wind tunnel, as described in Section 3.3.1. When the same geometry and test conditions that Latin used were input into FLUENT, the boundary layer thickness was within 10% of that measured by Latin. The two dimensional, double precision, coupled implicit solver was used for the test case and made use of the standard $k - \epsilon$ turbulence model equations.

Chapter 5 - Results and Discussion

This chapter contains the results of both the experimental and computational components of the present work. It contains quantitative comparisons of recorded and curve fit thermocouple data and qualitative flow structure comparisons from the computational results and schlieren photograph. A discussion of the Stanton number calculations is also included.

5.1 Experimental Results

The test conditions present at the time of testing are shown in Table 4.

Table 4. Test conditions

Test	P_0 (Pa) measured; see Figure 3	P (Pa) calculated	T_0 (K) measured; see Figure 3
Axial, Transverse	2.87E5	9.08E3	295
Flat Plate	2.91E5	9.22E3	294

Two separate tests of the inclined trailing wall insert were required based on the available thermocouple connections to the data acquisition system. First, an axial test was conducted, measuring the temperature history at stations 1-8. Second, a transverse test was conducted, measuring the temperature history at stations 1-3, 5 and 7-10. Care was exercised to ensure that the transverse and axial tests were conducted at the same flow conditions. Values of static pressure were determined from isentropic flow tables for air ($\gamma = 1.4$) at $M = 2.9$ [5].

5.1.1 Thermocouple Data

A comparison between the recorded temperature data for the inclined trailing wall insert and fit temperature data using equation (48) for station 5 is shown in Figure 15. The curve fit variables used in equation (48) were $\omega = 0.078 \text{ rad/sec}$, $A = 4.9 \text{ K}$ and a corrected temperature amplitude, $A_{corr} = 5.22 \text{ K}$. This figure shows good agreement during tunnel operation with $RMS = 6.09$ from equation (49).

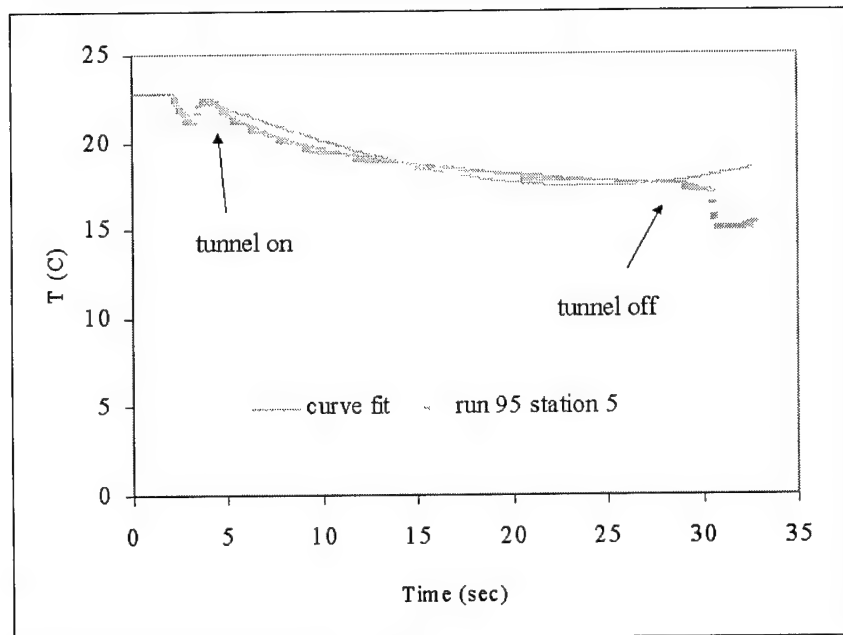


Figure 15. Comparison between fit and recorded data for inclined trailing wall; station 5

Figure 10 shows a comparison between the recorded temperature history at station 1 for the flat plate and the curve fit temperature data. The curve fit variables used in equation (48) were $\omega = 0.07 \text{ rad/sec}$ and $A = 5 \text{ K}$ with a corrected temperature amplitude, $A_{corr} = 5.31 \text{ K}$. This figure shows that the recorded and fit temperature histories are also in good agreement with $RMS = 3.96$ from equation (49).

The negligible radiation assumption requires further analysis. A radiosity formulation was the method used for this analysis [24,35]. Radiosity is defined as the rate of energy radiating from a surface by both emission and reflection. A radiosity formulation is useful when analyzing an enclosure, such as the case of the present work. This analysis modeled the plexiglas insert and surrounding optical glass as diffuse-grey surfaces; their radiant transport properties did not vary with direction or wavelength. The reflectivities of the enclosure walls were not considered in the enclosure analysis because these surfaces were assumed to obey Kirchhoff's Law

$$\alpha + \rho = \varepsilon + \rho = 1 \quad (54)$$

where α is the absorptivity and ρ is the reflectivity. With $\varepsilon_{plexi} = 0.95$ [28], the reflectivity becomes $\rho = 0.05$. Therefore, the radiant energy due to reflection was overshadowed by the radiant energy due to emission. The viewfactors were determined by analyzing a two dimensional slice through the cavity at the cavity insert and perpendicular to the flow direction. The emissivity for the optical glass windows in the ceiling and sidewalls was $\varepsilon = 0.9$ [19]. For the flat plate insert, the wall temperatures for all four walls were assumed to be at the same temperature as that recorded on the cavity insert. This was reasonable, considering that the boundary layers will develop at the same rate on all walls. Therefore, the radiation exchange between these surfaces was quite small, in fact, at station 1 and at station 8, $q''_{rad}/q''_{conv} = 5E-19$. For the inclined trailing wall insert, the entire insert was taken to be at a depth of 0.784 cm , thereby neglecting the trailing wall. Further-

more, the resulting viewfactor from the cavity floor to the aluminum rear facing step was assumed small compared to that to the sidewalls and was therefore neglected. The validity of this assumption was dictated by the end result. The insert surface temperature at station 1 will be higher than the other walls since the flow velocity was quite smaller there. This higher temperature causes the radiation exchange to be higher, yielding at station 1, $q''_{rad}/q''_{conv} = 0.0089\%$ and at station 8, $q''_{rad}/q''_{conv} = 0.0051\%$. However, these results were $\ll 1\%$, hence, radiation was neglected.

5.1.2 Shock Placement

The schlieren photograph yielded qualitative data about the flow structure in and around the cavity. Figure 16 shows the schlieren photograph containing $\partial\rho/\partial y$ information. Notice that the light colored boundary layer exists along the tunnel floor and through the shear layer, as discussed in Section 3.2.2.

The expected shock angle, β , for flow at $M = 2.9$ incident on a corner at $\theta = 20^\circ$ is 38.5° using oblique shock relations [5]. This is the weak shock solution as the back pressure was low enough to prevent the strong shock solution. The shock angle measured from Figure 16 is $29^\circ \pm 0.5^\circ$ and was measured from the shear layer to the shock. The reattachment point was measured to be $1.69\text{ cm} \pm 0.1\text{ cm}$, measured from the beginning of inclined trailing wall. This is shown in Figure 16 as the point where the lowest extreme of the shear layer intersects the inclined trailing wall. The flow structure shown in Figure 16 was present through the duration of tunnel operation. Therefore, the steady state assumption for the CFD analysis was reasonable (see Section 4.1). The shock from upper left to lower right shown in Figure 16 resulted from an unavoidable surface discontinuity at the ceiling-nozzle exit interface. The shock angle measurement suggests that the experimental results are not consistent with oblique shock theory. However, the difference between oblique shock theory and the experimental results presented here is due to two items. First, the

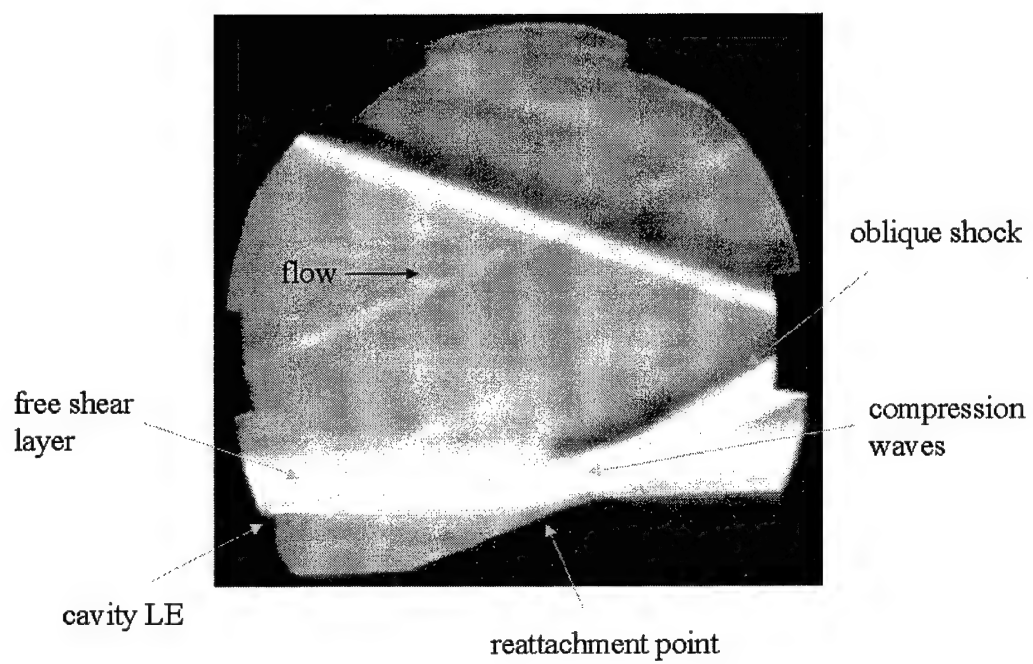


Figure 16. Schlieren photograph showing flow reattachment and oblique shock formation

Mach number upstream of the shock and above the cavity is higher than the freestream Mach number at the nozzle exit. This is discussed further in Section 5.2. Second, oblique shock theory does not account for boundary layer-shock interaction. This interaction causes the shock to bend downstream, starting at the shock origination point for wedge flow. In the current study, the shock wave bends up. This is due to the presence of a curved displacement surface at the top of the inclined trailing wall.

From Figure 16, it is clear that the flow coalesces into a shock from a series of compression waves above the reattachment point. Settles *et al.* [33] discuss that this occurs due to a gently curved displacement surface formed by the free shear layer during the reattachment process. This curved displacement surface is shown in the form of displacement thickness in Figure 17, notice that the thickness decreases along the inclined trailing wall.

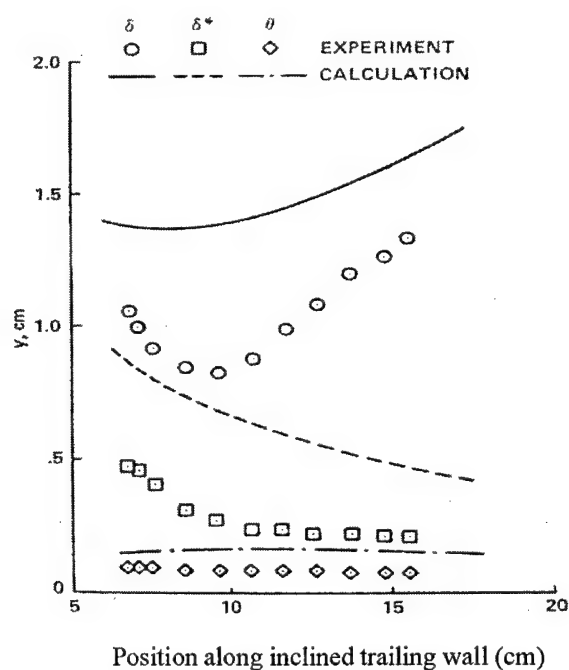


Figure 17. Integral values along inclined trailing wall; taken from Horstman *et al.* [17]

The displacement thickness for compressible flow, defined as [49],

$$\delta^* = \int_0^\infty \left(1 - \frac{\rho}{\rho_\infty} \frac{u}{u_\infty} \right) dy \quad (55)$$

is the small displacement of the outer streamlines away from the wall due to the boundary layer at the wall [21,48]. It can also be thought of as an extension of the wall, since no mass flow crosses the displacement thickness. Therefore, relative to the flow, the displacement thickness creates a new wall surface.

The upper limit in equation (55) can be replaced with the boundary layer thickness, δ , considering that, above this distance, $\rho = \rho_\infty$ and $u = u_\infty$ and therefore do not contribute to the integral. In the current work, the displacement surface created a curved surface which gradually turned the flow, causing small disturbance waves called Mach lines to converge into an oblique shock outside of the boundary layer [5]. For the present work, the displacement thickness was numerically integrated from the computational results using the trapezoid rule and is shown in Figure 18. The dip in Figure 18 at an axial position of 7.75 cm is a result of the interaction of the coalescing Mach waves and the boundary layer reattachment on the inclined trailing wall. Note that the displacement thickness gently decreases in a similar fashion as the results shown in Figure 17.

5.1.3 Stanton number correlation

The Stanton number calculations were performed using the curve fit data and equations (30) and (46). The value of specific heat used in equation (30) was determined using the film temperature, $T_f = (T_\infty + T_{w,ave})/2$ from the values presented by Incropera and DeWitt [19]. The variation of Stanton number with axial position for both cavity inserts is shown in Figure 19 with the cavity geometry included for clarity. The calculation of the error bounds is shown in Appendix A. As expected, the flat plate Stanton number decreases with axial distance from the nozzle exit. The two

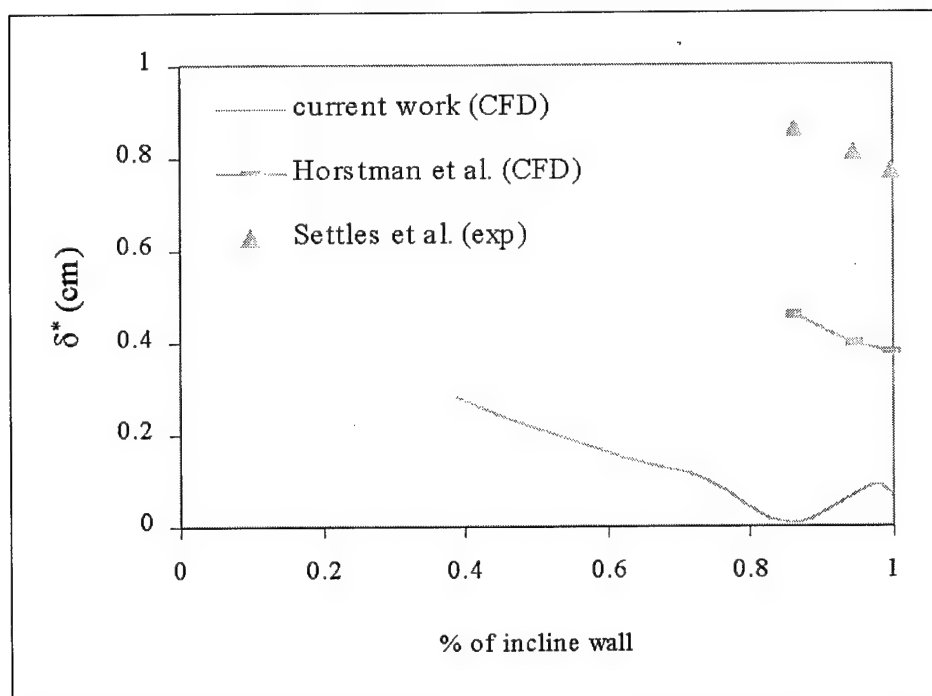


Figure 18. Displacement thickness along inclined trailing wall; CFD results

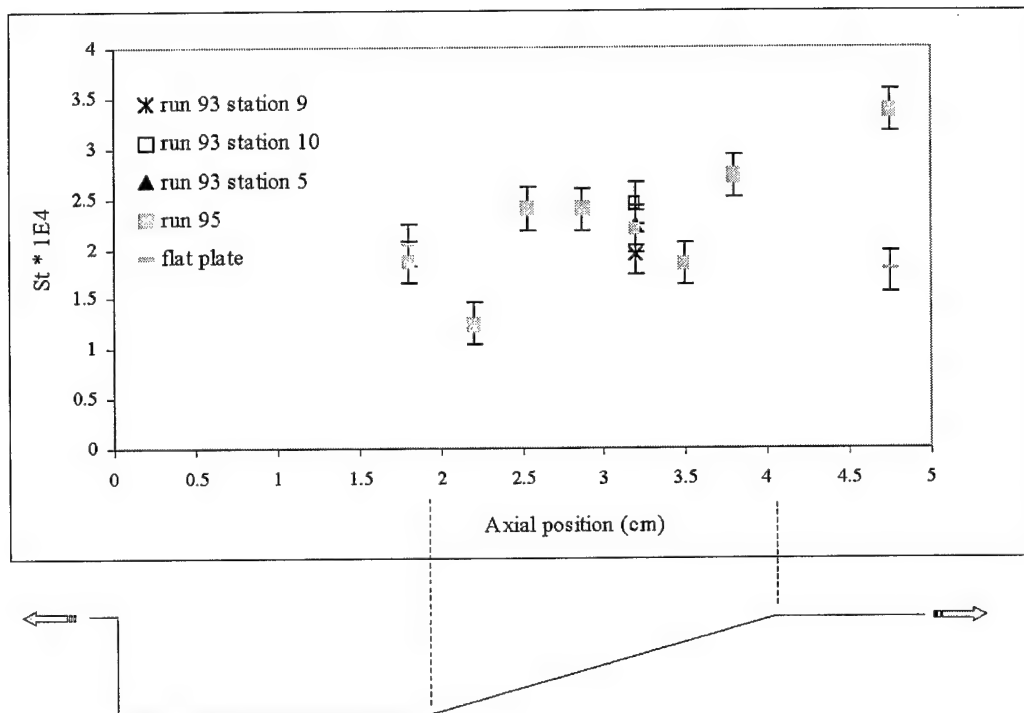


Figure 19. Stanton number variation with axial position for inclined trailing wall and flat plate inserts; experimental results

dimensional flow assumption requires that the Stanton numbers at stations 9 and 10 be virtually the same as that at station 5 since they are at the same axial position. A slight reduction in Stanton number at stations 9 and 10 would be expected due to conduction losses, but this should be symmetric about station 5. It appears that this is the case for station 9, but not for station 10. However, when the Stanton number uncertainty is included, the Stanton numbers for all three overlap. Upon further inspection of Figure 19, one will notice that the Stanton number at station 5 for run 95 and run 93 are nearly coincident. This indicates that the tests were repeatable and consistent. Additionally, one will notice that the Stanton numbers at station 1 are nearly the same for the flat plate and trailing wall inserts, while these numbers at station 8 are considerably different. The Stanton number downstream of the oblique shock was found to be 90% higher than that at the same axial location on the flat plate. This suggests that the increase was due to the shock-boundary layer interaction downstream of the inclined trailing wall. On the other hand, the Stanton number in the base of the cavity was 8% lower than that of the flat plate at the same axial location. This result suggests that the physical mechanism responsible for Stanton number decrease in the base of the cavity was due to flow recirculation in the cavity.

The variation of Stanton number shown in Figure 19 along the inclined trailing wall suggests that the physical mechanisms were recirculation, reattachment and stagnation flow effects. (Recall from Figure 16 that reattachment was determined to occur at 1.69 *cm* measured along the incline from the bottom of the inclined trailing wall or 3.71 *cm* measured axially from the cavity LE). The Stanton number increased 30% down the inclined wall from reattachment. This suggests that the increase was due to recirculation and its associated changing fluid velocity magnitude and direction. Ascending the inclined trailing wall from reattachment, the Stanton number increased nearly 50% between stations 6 and 7, with reattachment occurring between these stations. This suggests that the increase was due to the conversion of kinetic energy to thermal energy associated with turning

the flow at the inclined trailing wall. This increase in Stanton number due to flow turning can also be seen by moving with the recirculated flow from station 2 to station 1 where the Stanton number increased 50%. The cavity floor at station 1 represents a wedge with angle $\theta = 20^\circ$ to the flow moving down the inclined wall from station 2. An oblique shock wave did not result, however, because the magnitude of the local fluid velocity was lower than the local speed of sound. This subsonic flow can be seen in the Mach number variation in the cavity shown in Figure 23. The author believes that the decrease in Stanton number from station 3 to station 2 was due to the changing flowfield.

The heat transfer coefficient for the flat plate at station 1 corresponding to the Stanton number shown in Figure 19 can be used to predict a temperature history for comparison with the recorded temperature history. Figure 20 shows this comparison, where the predicted history was determined using equation (51) accounting for the thermocouple sensing displacement (see Section 3.5).

One will notice from this figure that the difference between the predicted and recorded histories were within the accuracy of the data acquisition equipment. Therefore, the data reduction method was considered accurate.

Final heat transfer coefficient values for the inclined trailing wall cavity were five times smaller than the value used in equation (45) for the cavity insert design. This difference is due to the boundary layer interaction; the inclined trailing wall was never directly exposed to the freestream Mach number. This lower heat transfer coefficient would cause Δy in equation (45) to be considerably larger. However, the depth of the cavity was still valid considering the short run time of the tunnel ($< 25 \text{ sec}$). This short time prevented the thermal wave from propagating to the bottom of the cavity, as determined by equation (51). Thus, the semi-infinite solid assumption was maintained. As a verification, the temperature at the bottom of the cavity was calculated using equation (51) resulting in a drop of only 0.02°C . The thermocouple used to verify temperature uniformity showed a drop

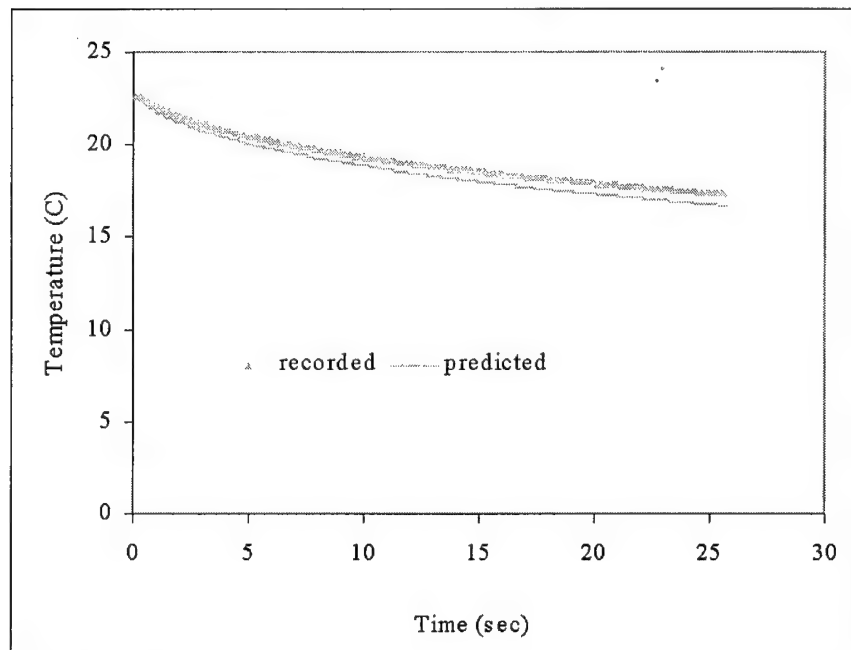


Figure 20. Comparison between predicted and recorded temperature histories for flat plate insert; station 1

of 0.2 C . The difference between the two methods was within the uncertainty of the measurement and was therefore neglected.

The final heat transfer coefficients for the flat plate were also lower than that determined in Section 3.3.1. This is due to the short distance between the nozzle exit and the cavity LE. As one might expect, the velocity boundary layer was developing considering this short distance. However, the thermal boundary layer was also developing since the Prandtl number was near unity for the current study. Heat transfer data on this arrangement of simultaneously developing flow in a square duct are limited, but not nonexistent. Emery *et al.* [13] performed a numerical analysis to predict the heat transfer and developing turbulent incompressible flow in a square duct for Pr near unity and $Re_{D_h} \leq 250,000$ for various wall heat flux treatments. Their results were compared to experimental data for the fully developed region with good agreement. Their findings showed that the boundary layers were fully developed at $x/D_h \geq 120$. For developing turbulent compressible flow, the literature contains primarily flowfield data in the developing region, such as velocity profiles and skin friction data. Davis and Gessner [12] conducted flowfield measurements on developing turbulent compressible flow of air at $M = 3.9$ and $Re = 2E7 \text{ m}^{-1}$ for $0 \leq x/D_h \leq 50$. Although the Mach number for their study was higher than that from the current study, the unit Reynolds number was the same, so the results are comparable. Davis and Gessner determined that the the boundary layers nominally began to merge at $x/D_h = 30$. Clearly, given this value, the boundary layers in the current study were still developing at station 1 ($x/D_h = 0.92$) and station 8 ($x/D_h = 1.4$) where the flat plate heat transfer was determined. The skin friction coefficient data from Davis and Gessner show a decreasing trend with decreasing x/D_h . Thus, extrapolating the skin friction coefficient results to $x/D_h \approx 1$ and assuming a Reynolds type analogy is applicable ($St = \frac{1}{2} c_{f\infty} Pr^{-\frac{2}{3}}$ [41]), the Stanton results from the current study were on the same order as that from Davis and Gessner. Additionally, the difference between the flat plate results and the flat

plate calculation from Section 3.3.1 can also be seen in the formulation of the flat plate correlations. These correlations assumed a $\frac{1}{7}$ power velocity distribution which agrees well with experiment [32], whereas the square duct used in the current study contained vortical flow in the corner regions which altered the primary flow [12]. This vortical flow can not be modeled so simply. Considering this difference and the comparison with the experimental results of Davis and Gessner, the flat plate insert results were considered reasonable. Note, skin friction coefficient data from the current study was not available for comparison as these data were not taken. Similarly, the CFD results could not be compared as the streamwise extent of the CFD domain was $x/D_h = 9.4$ and the closest location from Davis and Gessner's work was $x/D_h = 20$.

5.2 Computational Results

This section contains results from the CFD analysis for both the flat plate and inclined trailing wall simulations.

5.2.1 Flat Plate Insert

The Stanton number variation with position for the flat plate insert is shown in Figure 21. This too shows the correct trend; decreasing Stanton number with increasing distance from the nozzle exit. More importantly, the results shown in Figure 21 correlate well with the flat plate experimental results shown in Figure 19, with less than a 10% difference at both station 1 and 8. This agreement lends credibility to the use of the curve fit method described in Section 3.5 since this model produced results with good agreement to the boundary layer measurements performed by Latin [22] (see Section 4.5).

5.2.2 Inclined Trailing Wall Insert

The oblique shock placement can be seen in Figure 22 based on pressure gradients above and downstream of the top of the inclined trailing wall. Using Figure 22, the shock angle was measured

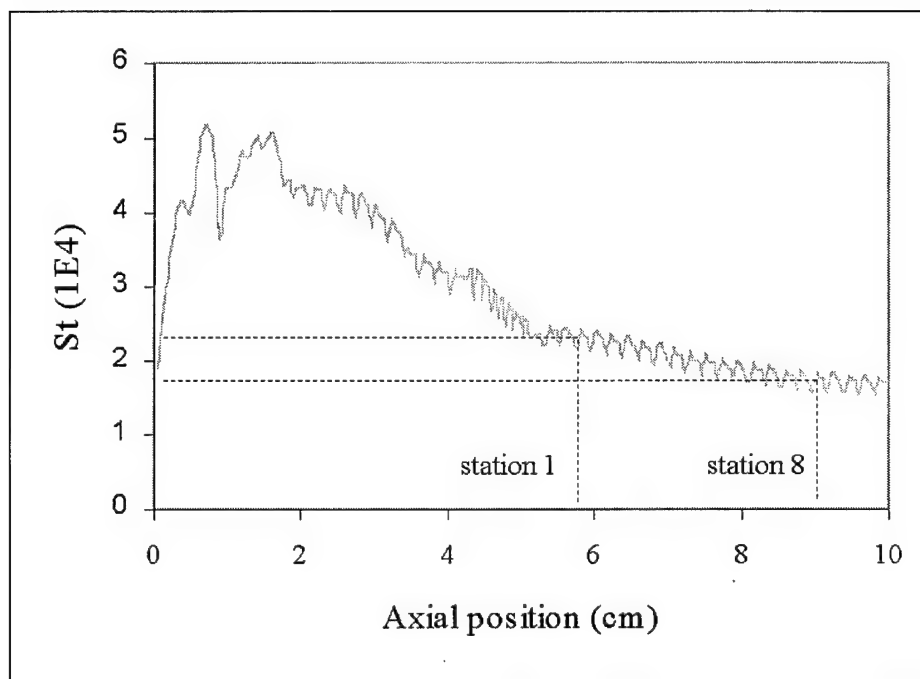


Figure 21. Stanton number variation with axial position for flat plate; CFD results

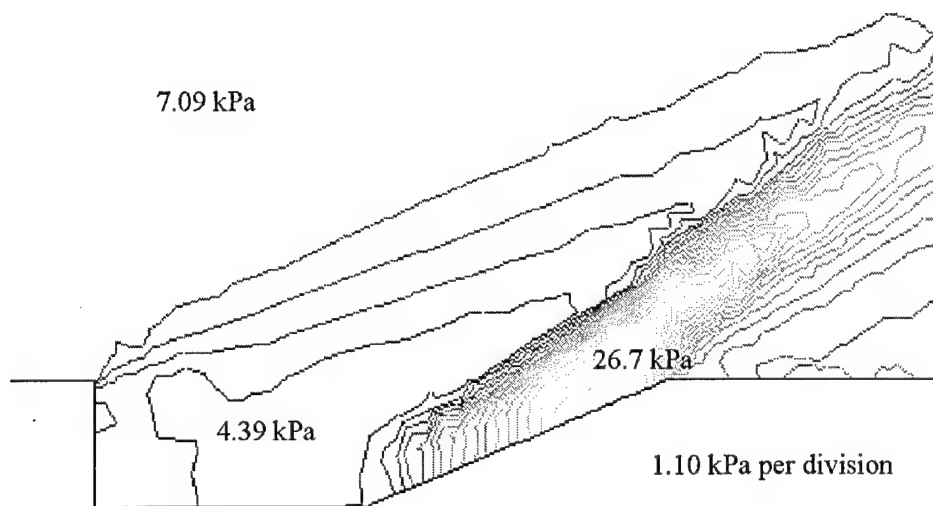


Figure 22. Pressure distribution through cavity; CFD results

to be $\beta = 40^\circ \pm 2^\circ$, which is consistent with oblique shock theory. As discussed in Section 5.1.2, a higher Mach number exists just above the cavity (see Figure 23) Using this higher Mach number,

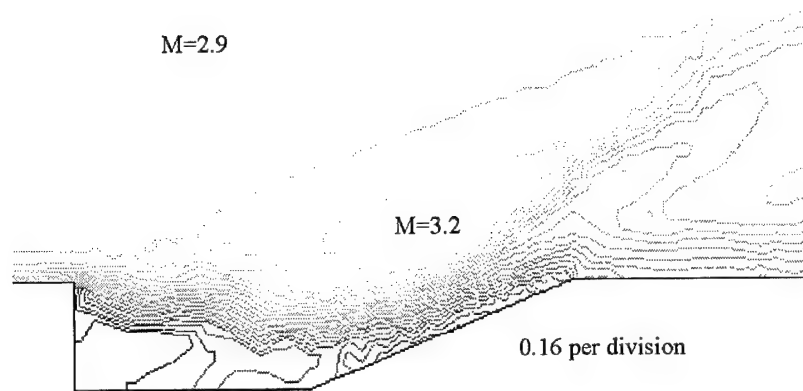


Figure 23. Mach number distribution through cavity; CFD results

$M = 3.2$, the shock angle is $\beta = 35^\circ$ [5], which is closer to the experimental value. However, this large difference from the experimental measurement results from reattachment occurring farther down the trailing wall than that from the experiment due to an inadequate turbulence model (see Figure 27 for reattachment point based on c_f values).

Figure 24 shows the temperature distribution through the cavity. Note the large gradients at the top of and downstream of the inclined trailing wall.

The Stanton number variation with position for the inclined trailing wall insert is shown in Figure 25. This figure shows the same trend as the experimental results, but with a large reduction in magnitude within the cavity. This reduction is likely due to the turbulence model used for the CFD analysis. This topic is covered more completely in Section 5.3.

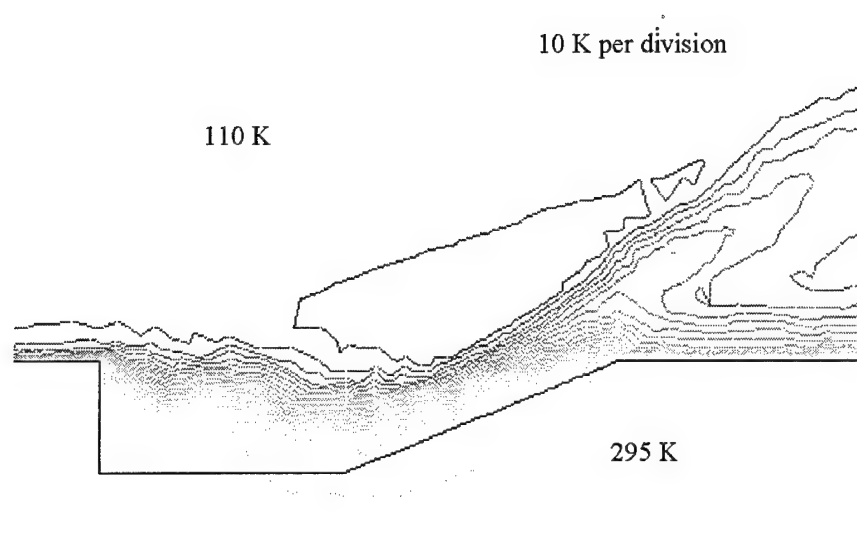


Figure 24. Static temperature distribution through cavity; CFD results

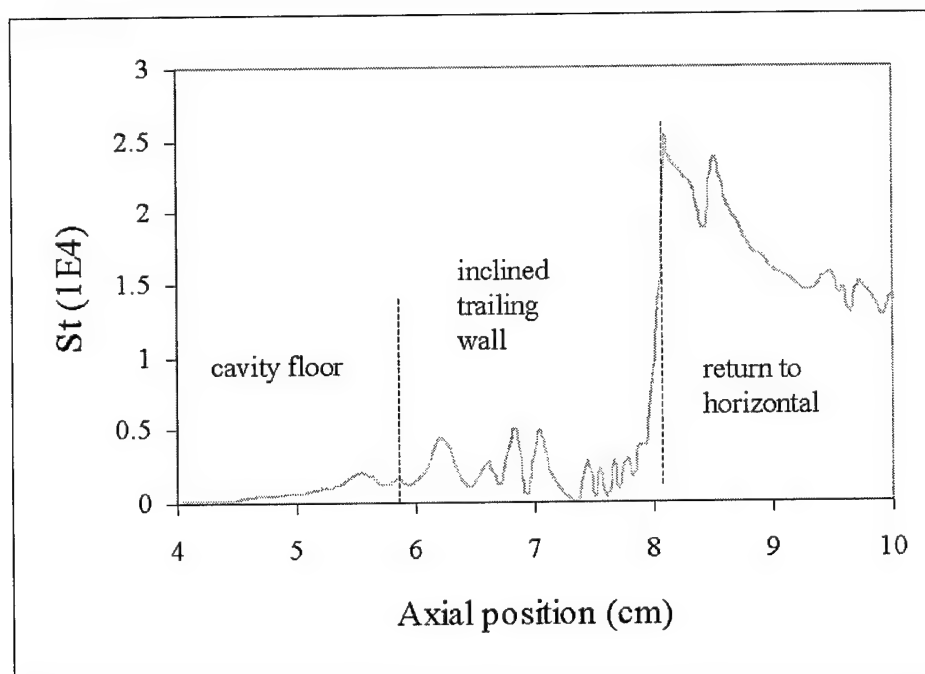


Figure 25. Stanton number variation with axial position; CFD results

The shear layer reattachment point is one method of comparing the present results with the open literature. Horstman *et al.* [17], in their computational model, determined the reattachment point to be at a distance of 5.2 *cm* which was measured along the inclined wall, originating at the cavity floor-inclined wall junction. This value corresponds to 1.6 *cm* for the present work and was determined by comparing the reattachment point-to-inclined wall length ratio. This method of comparison is reasonable considering the findings of Samimy *et al.* [31], stating that, after comparison with other experiments involving free shear layers, the geometry downstream of reattachment has little affect on the reattachment process. The present computational results have reattachment occurring at 1.25 *cm* (see Figure 27), measured from the bottom of the inclined trailing wall, which is close to the 1.6 *cm* value shown above.

A plot of velocity vectors in the cavity, Figure 26, reveals that the maximum reverse velocity is $0.27u_{\infty}$, and is located where the pressure is a minimum, see Figure 22. One clockwise recirculation zone exists in the cavity, with flow returning to the rear facing step. This result is similar to that obtained by Horstman *et al.* [17] and Samimy *et al.* [31] and will be discussed in more detail in Section 5.3.

The skin friction coefficient for the inclined trailing wall through the reattachment region is shown in Figure 27. This figure also includes the experimental research of Settles *et al.* [33] and the computational research of Horstman *et al.* [17] who performed a computational study based on the results of Settles *et al.* [33]. The reattachment point is where the skin friction coefficient is zero for both the CFD analysis and experimental measurement from the comparative study. For the current study, the approximate reattachment point was determined from the schlieren photograph. This is evident from the definition of the skin friction coefficient,

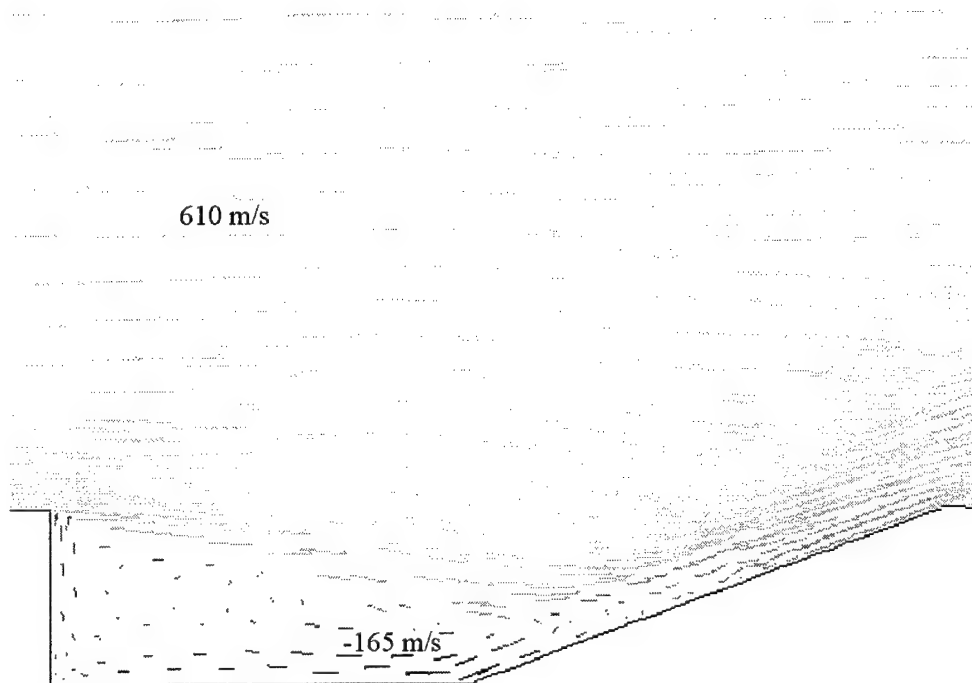


Figure 26. Velocity vectors through cavity; CFD results

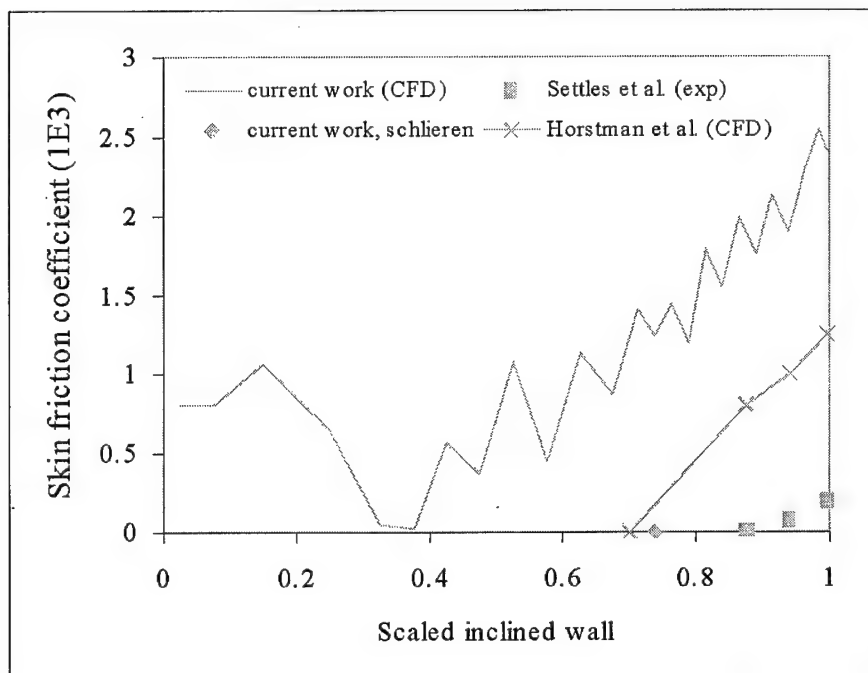


Figure 27. Skin friction coefficient variation along inclined trailing wall

$$c_f = \frac{\tau_w}{\frac{1}{2}\rho V^2} \quad (56)$$

and that the shear stress goes to zero at a stagnation point because the fluid is normal to the surface. The current values of skin friction coefficient display the same trend as that from Horstman *et al.* [17]. Note the difference in the reattachment point determination by experimental and computational means. The reason for this difference is related to the choice of turbulence model as discussed further in Section 5.3.

One final comparison from the CFD results. The turbulent velocity boundary layer thickness at the cavity LE was calculated to be within 10% of that determined from equations (40-42). This lends confidence that the cavity in the computational domain was exposed to an equivalent flow structure upstream of the cavity.

5.3 Experimental and Computational Comparisons

Combining the flat plate results from Figures 19 and 21, Figure 28 shows that there was good agreement between the experimental and computational Stanton numbers, thus validating the use of the standard $k - \epsilon$ turbulence model for the flat plate case.

The agreement between the experimental and computational data for the inclined trailing wall insert was not as good, as shown in Figure 29. In examining this figure, the CFD Stanton number results in the base of the cavity were an order of magnitude lower than the experimental results and, at station 8, the CFD Stanton number was 40% low. The fact that there is such poor agreement in Stanton number through the cavity suggests that the realizable $k - \epsilon$ model may not be an acceptable turbulence model for the cavity flow field.

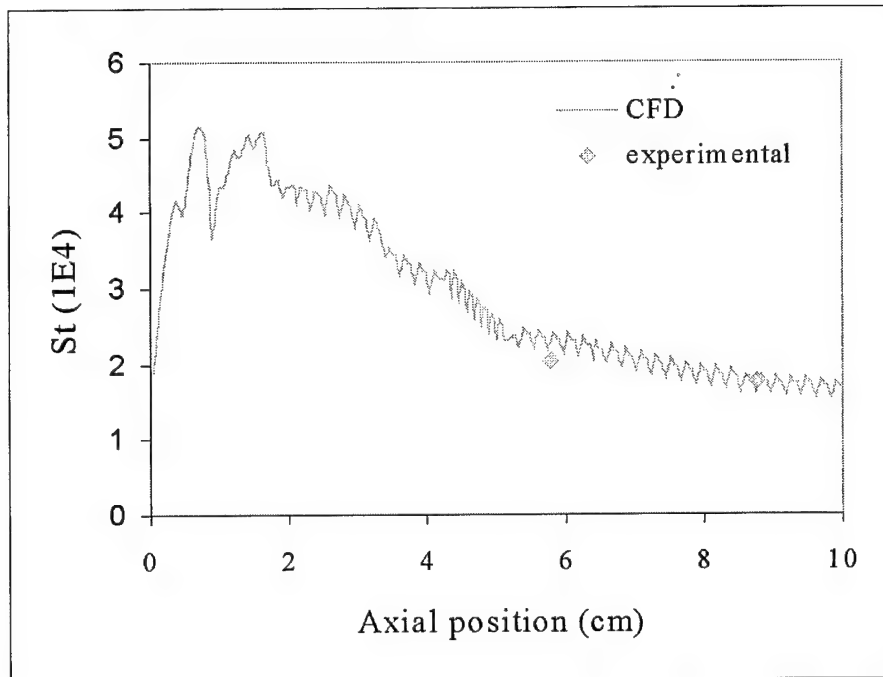


Figure 28. Comparison of Stanton number for flat plate insert; CFD and experimental results

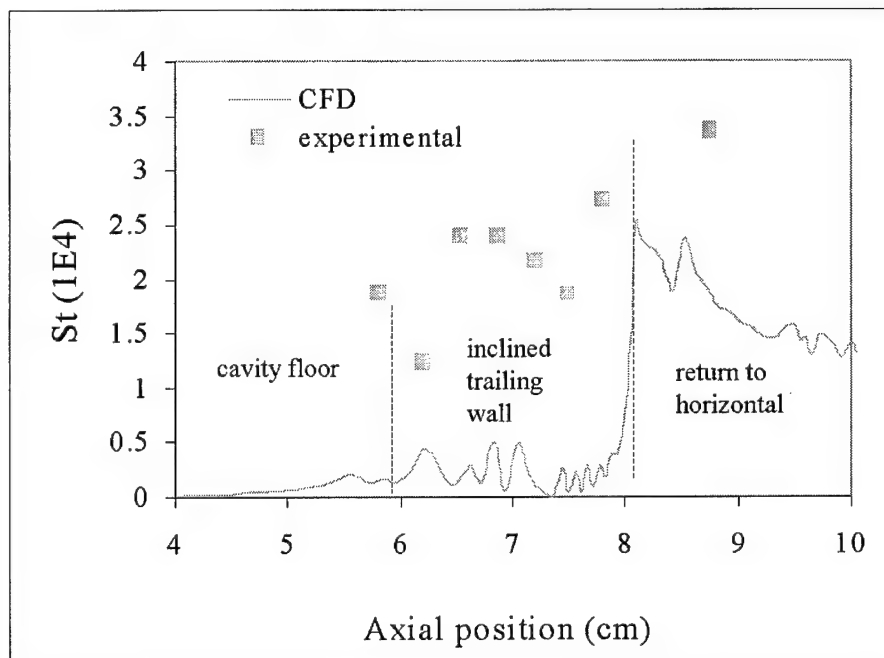


Figure 29. Comparison of Stanton number for inclined trailing wall; CFD and experimental results

Table 5 shows a comparison between some experimental and computational results from the current work and those of other researchers. The cavity geometries for the various researchers shown in Table 5 were all similar to the current geometry. The table indicates that the turbulence models used to analyze cavity flows to date were not adequate. The skin friction coefficient range, Stanton number range and reattachment point all vary from the experimental results. The skin friction coefficient results of Horstman *et al.* [17] and Settles *et al.* [33] exhibit the same order of magnitude difference between computational and experimental results as the Stanton number results of the current study but in an opposite direction. This difference was attributed to an inadequate turbulence model in the current study.

Table 5. Comparison of results with the literature

Item	Test	AFIT	Horstman <i>et al.</i> [17]	Samimy <i>et al.</i> [31]
Reattach point;	Exp	74	91 [33]	76
% of incline	CFD	37	70	n/a
c_f range	Exp	n/a	0 – 1.3E-4 [33]	n/a
	CFD	0 – 2.5E-3	0 – 1.3E-3	n/a
St range	Exp	1.2E-4 – 3.4E-4	n/a	n/a
	CFD	~ 0 – 2.5E-4	n/a	n/a
Number of	Exp	n/a	n/a	1 cw
recirc zones	CFD	1 cw	1 cw	n/a
Max. reverse vel	Exp	n/a	n/a	0.2 u_∞
	CFD	0.27 u_∞	0.17 u_∞	n/a

This apparent lack of an appropriate computational model of cavity flow can also be seen in the results of Weinberg *et al.* [46] who performed a CFD analysis based on the experimental research of Settles *et al.* [33]. The results of Weinberg *et al.* showed three recirculation zones (2 cw; 1 ccw) in the cavity which vastly differs from the results of Horstman *et al.* [17], who also performed a computational comparison to the experimental results of Settles *et al.* [33]. However, the CFD analysis performed by Horstman *et al.* [17] did not accurately predict the skin friction coefficient on the inclined trailing wall, as shown in Figure 27. The differences between CFD and

experimental results in each of these papers were noted by their respective authors, concluding that modification or further evaluation of the turbulence model is required to more accurately analyze cavity flows. Consequently, cavity flow researchers have used a variety of turbulence models in an effort to determine an acceptable model. This is evident by the various turbulence models used for cavity flows, as shown in Table 6.

Table 6. Turbulence models used to examine cavity flows

Researcher	Turbulence model
AFIT	realizable $k - \epsilon$
Horstman <i>et al.</i> [17]	Wilcox-Rubesin
Weinberg <i>et al.</i> [46]	standard $k - \epsilon$
Shih <i>et al.</i> [34]	coupled $k - \epsilon$
Davis and Bowersox [10], [11]	Baldwin-Lomax
Tam <i>et al.</i> [37]	Baldwin-Lomax

A brief discussion about the various turbulent models shown in Table 6 is included here (see Section 4.2.1 for more on the realizable $k - \epsilon$ model). Additional partial differential equations augment the two equations for turbulence kinetic energy and the square of the dissipation rate used in the Wilcox-Rubesin model. Furthermore, this model uses the eddy-viscosity hypothesis which simply adds an eddy transport coefficient to the corresponding molecular viscosity or transport coefficient [17]. Weinberg *et al.* [46] utilized the familiar $k - \epsilon$ equations with a modification of wall treatment based on transition in the boundary layer. The coupled $k - \epsilon$ model used by Shih *et al.* [34] was based on changes in both pressure and turbulent kinetic energy. This coupling was done to establish an appropriate numerical procedure to couple the Navier-Stokes and $k - \epsilon$ equations for use in simulating unsteady flow. The Baldwin-Lomax turbulence model, developed for separated flows, algebraically models turbulence in two layers; an inner layer dominated by shear force at the wall and an outer layer that is mainly influenced by the wake of upstream forces [9]. The research

performed by Tam *et al.* [37] included several modifications of the Baldwin-Lomax model, such as modeling laminar flow in and above the cavity.

The fact that there have been various approaches to the turbulence closure problem confirms that an appropriate turbulence model has not as yet been found. This was echoed by Shih *et al.* [34] and Tam *et al.* [37]. Both of these authors compared their results to experimental data with the same conclusion; no one model accurately predicts the flow structure or properties within the cavity.

Chapter 6 - Conclusions and Recommendations

This chapter contains several conclusions based on the current work as well as recommendations concerning directions for future research.

6.1 Conclusions

Heat transfer data in the form of Stanton number were determined for a cavity geometrically similar to one under review for use in a scramjet engine. The cavity is being considered based on a need to increase fuel/air residence time and provide flame holding in the combustor. To this end, the current study sought to perform two tasks: to increase the heat flux data base for cavity flows and to describe the physical mechanisms occurring in the cavity flowfield.

The cavity geometry design incorporated an inclined trailing wall, providing recirculation while minimizing the heat flux load to the trailing wall. The Stanton number was calculated using recorded surface temperature data. These data were compared to that using recorded surface temperature data for the same flow over a flat plate, as well as to that from a computational model. Lastly, the flow structure was qualitatively compared between computational results and flow visualization. The following conclusions are presented based on the data.

1. *Heat transfer downstream of the cavity was increased by nearly 90% compared to that of a flat plate.* At the same axial distance from the nozzle exit, the Stanton number calculated downstream of the cavity was increased by 90% than that for the flat plate. This suggests that the increase in heat transfer was due to the boundary layer-shock interaction that existed at the inclined trailing wall. Additionally, the temperature results shown in Figure 24 and the Stanton number results shown in Figures 19 and 25 indicate an area requiring particular attention. The top of the inclined trailing wall where the highest heat flux loads occurred would require specific

consideration with regard to thermal management and design of the operational cavity. In fact, in recent hot flow tests conducted by HyTech, the cavity wall melted at this location [44].

2. *Heat transfer in the base of the cavity was roughly the same as that on a flat plate at the same axial position.* As shown in Figure 24, the vertical temperature gradients in the base of the cavity were smaller than those upstream of the cavity. However, the fluid velocity in the cavity was lower as well. The combination of these two changes resulted in little change in heat transfer coefficient (see equation (33)) and consequently, little change in the Stanton number.

3. *The heat transfer coefficient for the flat plate was lower than anticipated.* The Stanton number for stations 1 and 8 was approximately 5 times lower than that calculated using flat plate correlations at the same axial locations. This difference was due to the simultaneous development of both the velocity and thermal boundary layers caused by the Prandtl number being near unity and the close position of the cavity to the nozzle exit. This difference was also seen in the formulation of the flat plate correlations. These correlations assumed a $\frac{1}{7}$ power velocity distribution. The square duct used in the current study contained vortical flow in the corner regions which altered the primary flow and could not be modeled so simply.

4. *Heat transfer along the inclined trailing wall varied based on position relative to the reattachment point.* Figure 19 shows that heat transfer increased 30% descending the inclined trailing wall from the reattachment point. This result suggests that flow recirculation with its associated changes in fluid velocity magnitude and direction was the responsible physical mechanism. Figure 19 also shows that heat transfer was enhanced by nearly 50% ascending the inclined wall from reattachment. This result suggests that the conversion of kinetic energy to thermal energy was the responsible physical mechanism. The conversion of energy occurred due to the flow turning at the inclined trailing wall. This increase in Stanton number based on flow turning can also be seen by moving with the recirculated flow from station 2 to station 1 where the Stanton number was in-

creased 50%. The cavity floor at station 1 resembled a wedge with angle $\theta = 20^\circ$ relative to the flow moving down the inclined trailing wall.

5. *A curved displacement surface at the inclined trailing wall caused small compression waves to coalesce into an oblique shock.* The reattachment process at the inclined trailing wall caused a gently curved surface to exist on the inclined trailing wall based on the displacement thickness. This surface gradually turned the flow, causing weak compression waves to coalesce into an oblique shock above the reattachment point. These compression waves were visible in the schlieren photograph, while the curved displacement thickness surface was obtained from the CFD results. This curved surface was also visible in the experimental results of a referenced article using a geometrically similar cavity.

6. *The turbulence model did not accurately capture the cavity flow field.* A comparison between the CFD and experimental results suggests that the large difference between the calculated Stanton number results in the cavity was primarily due to an inaccurate turbulence model. This result was echoed by many other researchers, concluding that an appropriate turbulence model for reattaching, compressible shear layer flows poses an obstacle for turbulence modelers. Cavity flow fields are simply not well understood.

7. *Computational models should be supported by experimental data.* The results shown in Figures 17 and 27 illustrate the differences between experimental and computational studies. Typically, computational results will trend the same as the experimental results, but often vary in magnitude. These variances may be as high as an order of magnitude, as in the case of the Stanton number results in the base of the cavity. The large differences between the CFD and experimental results for the current work, as well as those articles referenced, suggest that computational models, as stand alone devices, should not be used to describe physical behavior. This is especially evident when analyzing cavity flows. Rather, computational models should be used as a tool which is

economical; providing usefulness in obtaining preliminary results before partial or full scale testing. This allows research to focus into areas unknown or not well understood. Therefore, experimental testing is critical to complete the analysis. Furthermore, experimental results can be used to develop better, more accurate turbulence models.

6.2 Recommendations

Several recommendations for future research activities are presented here.

First, considering that the operational scramjet propulsion system will have fuel injection, the addition of fuel injection upstream of the cavity or within the cavity would more accurately model the operational case. This fuel injection could have a profound impact on the flow structure based on previous work by Orth and Cameron [27]. Their results showed that the recirculation zone was greatly affected by injection at the rear facing step. Reddecliff and Weber [29] and Tishkoff *et al.* [39] discuss that future operational scramjet engines could use hydrogen or hydrocarbon fuels. Hydrogen fuel can be accurately simulated using helium, while hydrocarbon fuels can be accurately simulated using argon [43]. AFIT's Mach 2.9 wind tunnel can be readily adapted to accept injection with minimal modifications. New research activity involving fuel injection should not only include surface temperature readings, but also flow visualization to record the flow structure.

Second, flow through the combustor for the operational scramjet will occur over a range of Mach number and stagnation temperature and pressure. Therefore, further heat transfer experiments should be performed to determine what effect varying these parameters have on heat transfer through the cavity.

Third, flowfield measurements such as skin friction and fluid velocity along the inclined wall would provide additional information concerning the flow structure inside the cavity. These measurements, together with the Stanton number calculations, would lend insight into the coupling of

heat transfer and flow structure in the cavity through the use of a Reynolds-type heat transfer analogy.

Fourth, a change to the turbulence model is in order. Various models have been studied with varying degrees of success. A more accurate turbulence model has been shown in the present and cited works to be the link to finding an acceptable match between computational and experimental results. Considering the simplicity of the computational domain of the current study, time considerations associated with implementing an existing turbulence model would be minimal. Conversely, development and implementation of a new model would be quite involved.

Fifth, a change in mesh density may also be in order. Although y^+ values were monitored along the walls during the solution process, this doesn't guarantee that the mesh was the appropriate density. The question of grid refinement has been addressed before by other cavity flow investigators, such as Weinberg *et al.* [46] who realized that the differences with experimental data were due in part to grid density.

As is the case with most investigations, questions often arise that are related to, but are removed from, the current research area. This was the case with the heat transfer calculation over the flat plate insert. This leads to the sixth, and final, recommendation. Considering the limited research in simultaneously developing square duct flow, more research activity in this area would extend the heat flux data base and provide details about developing boundary layers. This information could prove useful to scramjet inlet design where boundary layer flow through the engine first develops. The AFIT Mach 2.9 wind tunnel would be an ideal facility to conduct this research considering the close proximity of the cavity to the nozzle exit, the flow visualization equipment and the existing ability of the tunnel ceiling to accept flowfield measurement equipment, i.e. hot wire anemometry and Preston probes.

APPENDIX A - Uncertainty Analysis

The uncertainty analysis for the calculation of the Stanton number at station 5 is shown in Table 7. To better capture the uncertainty of the acquisition system, the measured surface temperatures were all biased up and down by a constant value from the measure data. Also, a random value between zero and the instrument accuracy was added to the measured surface temperatures. These three methods would then capture the complete surface temperature fluctuation within the data acquisition system.

Wheeler and Ganji [47] suggest a “best estimate” for the uncertainty, w_R , of a measured quantity, R , is given by

$$w_R = \left[\sum_{i=1}^n \left(w_{x_i} \frac{\partial R}{\partial x_i} \right)^2 \right]^{\frac{1}{2}} \quad (\text{A-1})$$

where x_i denotes the variables used in the calculation of R and w_{x_i} represents the error bound for each variable x_i . Due to the use of a curve fit to the recorded temperature history, the partial derivatives in equation (A-1) were replaced with [25]

$$\frac{\partial R}{\partial x_i} \approx \frac{\Delta R}{\Delta x_i} \quad (\text{A-2})$$

where Δx_i is the perturbation in the instrument (see Table 7) and ΔR is the resulting change in the Stanton number. Moffat [25] describes that this substitution is appropriate for use with computer based data reduction schemes similar to the one in the current study. The effect on the calculated result for each instrument was determined by taking the absolute value of the difference between the calculated Stanton number using the fit data and the calculated Stanton number using the perturbed quantities. The magnitude of the perturbation must be equal to or less (for non-linear terms

such as T_w , see equations (46) and (48)) than the order of the instrument accuracy since this represents the error of the instrument [25].

The perturbation, Δx_i , for the surface temperatures was 1 C, which was on the same order as the accuracy of the data acquisition system. The freestream Mach number was perturbed by 0.05 and the TC depth was perturbed by $1.27E - 5$ m. The values in the Uncertainty column of Table 7 represent the product of the Instrument Accuracy (w_{x_i}) column and the Effect on Calculated Result column ($|calculated - new|$), where *calculated* represents the calculated Stanton number using the fit data and *new* represents the calculated Stanton number using the perturbed values. The Total Uncertainty was determined using equation (A-1), where the values from the Uncertainty column were approximately equal to $w_{x_i}(\partial R/\partial x_i)$ per equation (A-2).

Table 7. Uncertainty analysis for Stanton number calculation; station 5

Instrument	Units	Instrument Accuracy	Effect on Calculated Result (1E4)	Units	Uncertainty (1E4)
M_∞	-	0.053	0.097	($\Delta M = 0.05$)	0.00514
T_w (bias down)	C	1.3	0.066	1/(0.5C)	0.0858
T_w (bias up)	C	1.3	0.063	1/(0.5C)	0.0819
T_w (random)	C	1.3	0.045	1/(0.5C)	0.0585
T_0	C	1.3	0.125	1/(0.5C)	0.163
p_0	Pa	900	0	1/(500Pa)	0
p_∞	Pa	31	0	1/(10Pa)	0
TC depth	m	$2.54E - 5$	629	1/(m)	0.0160
				Total	
				Uncertainty	0.211

Bibliography

- [1] Abuaf, N., Bunker, R. S. and Lee, C. P. "Effects of Surface Roughness on Heat Transfer and Aerodynamic Performance of Turbine Airfoils." *Transactions of the ASME* 97-GT-10. Presented at the International Gas Turbine & Aeroengine Congress & Exhibition, Orlando FL, June 2-5, 1997.
- [2] Alfahaid, A. F., Mohieldin, T. O. and Tiwari, S. N. "On the Characteristics of Turbulent Multiple Jets Diffusion Flame: Part I, Cold Flow." *AIAA* paper 97-2586.
- [3] "Analytical and Experimental Evaluation of the Supersonic Combustion Ramjet Engine." Technical Report AF APL-TR-65-103. Volume II. Air Force Aero Propulsion Laboratory, Research and Technology Division, Air Force Systems Command, December 1, 1965.
- [4] "Analytical and Experimental Investigation of the Low Speed Fixed Geometry Supersonic Combustion Ramjet." Technical Report AFAPL-TR-66-102. Volume II. General Applied Science Laboratories, Inc., January, 1967.
- [5] Anderson Jr, J. D. *Modern Compressible Flow with Historical Prospective*. New York: McGraw-Hill, Inc. 2nd ed., 1990.
- [6] Arpaci, V. S. *Conduction Heat Transfer*. Reading MA: Addison-Wesley Publishing Company, 1966.
- [7] Baumeister, T., Avallone, E. A. and Baumeister III, T. eds. *Marks' Standard Handbook for Mechanical Engineers*. New York: McGraw-Hill, Inc. 8th ed., 1978.
- [8] Bejan, A. *Convection Heat Transfer*. New York: John Wiley & Sons, Inc. 2nd ed., 1995.
- [9] Davis, D. L. *Numerical Analysis of Two and Three Dimensional Recessed Flame Holders for Scramjet Applications*. Ph.D. Dissertation. AFIT/DS/ENY/96-12. School of Engineering, Air Force Institute of Technology (AU), Wright-Patterson AFB OH, September, 1996.
- [10] Davis, D. L. and Bowersox, R. D. W. "Computational Fluid Dynamics Analysis of Cavity Flame Holders for Scramjets." *AIAA* paper 97-3270. Presented at the 33rd AIAA/ASME/SAE/ASEE/ Joint Propulsion Conference and Exhibit, Seattle WA, July 6-9, 1997.
- [11] Davis, D. L. and Bowersox, R. D. W. "Stirred Reactor Analysis of Cavity Flame Holders for Scramjets." *AIAA* paper 97-3274. Presented at the 33rd AIAA/ASME/SAE/ASEE/ Joint Propulsion Conference and Exhibit, Seattle WA, July 6-9, 1997.
- [12] Davis, D. O. and Gessner, F. B. "Further Experiments on Supersonic Turbulent Flow Development in a Square Duct." *AIAA Journal*, Vol 27 No. 8, 1023-1030, August, 1989.
- [13] Emery, A. F., Neighbors, P. K. and Gessner, F. B. "The Numerical Prediction of Developing Turbulent Flow and Heat Transfer in a Square Duct." *Journal of Heat Transfer. Transactions of the ASME*, Vol. 102, 51-57 February, 1980.

- [14] *FLUENT 5 User's Guide*. Lebanon NH: Fluent, Inc., July, 1998.
- [15] Gruber, M. AFRL/PRSS, Wright-Patterson AFB OH. Personal communication. 1999.
- [16] Hill, P. and Peterson, C. *Mechanics and Thermodynamics of Propulsion*. Reading MA: Addison-Wesley Publishing Company 2nd ed., 1992.
- [17] Horstman, C. C., Settles, G. S., Williams, D. R. and Bogdonoff, S. M. A "Reattaching Free Shear Layer in Compressible Turbulent Flow." *AIAA Journal*, Vol. 20 No. 1, 79-85, January, 1982.
- [18] Huffman, R. E. *Mach 2.9 Investigation into the Flow Structure in the Vicinity of a Wrap-Around Fin*. MS Thesis. AFIT/GAE/ENY/95D-13. School of Engineering, Air Force Institute of Technology (AU), Wright-Patterson AFB OH, December, 1995.
- [19] Incropera, F. P. and DeWitt, D. P. *Fundamentals of Heat and Mass Transfer*. New York: John Wiley & Sons, Inc. 3rd ed., 1990.
- [20] *instruNet User's Manual*. Stamford CT: Omega Engineering, April, 1998.
- [21] Kays, W. M. and Crawford, M. E. *Convective Heat and Mass Transfer*. New York: McGraw-Hill, Inc. 3rd ed., 1993.
- [22] Latin, R. M. *The Influence of Surface Roughness on Supersonic High Reynolds Number Turbulent Boundary Layer Flow*. Ph.D. Dissertation. AFIT/DS/ENY/98M-02. School of Engineering, Air Force Institute of Technology (AU), Wright-Patterson AFB OH, March, 1998.
- [23] McConnaughey, P. K. and Andrews, C. D. "Flow Characterization of Enabling Technologies for Advanced Propulsion Development: CFD Analysis and Cold Flow Testing at NASA/Marshall Space Flight Center." *AIAA* paper 95-3126.
- [24] Menart, J. "ME 738 class notes." Wright State University, Fairborn OH, 1997.
- [25] Moffat, R. J. "Contributions to the Theory of Single-Sample Uncertainty Analysis." *Transactions of the ASME Journal of Fluids Engineering*, Vol. 104, 250-260 June, 1982.
- [26] *NASA Hyper-X Hypersonic Aircraft Program*. Technical Report, www.dfrc.nasa.gov/Projects/HyperX/index.html: NASA Langley Research Center, 1998.
- [27] Orth, R. C. and Cameron, J. M. "Flow in the Recirculation Zone in a Step-Type Supersonic Combustor." AD529274. October-December, 1973.
- [28] *Raytek User's Guide for the Raytek Infrared Pyrometer*. Raytek, Inc., April, 1997.
- [29] Reddecliff, J. and Weber, J. "Development and Demonstration of a Hydrocarbon Scramjet Propulsion System." *AIAA* paper 98-1613. Presented at the 8th International Space Planes and Hypersonic Systems and Technology Conference, Norfolk VA, April 27-30, 1998.

- [30] Roshko, A. and Thomke, G. J. "Observations of Turbulent Reattachment Behind an Axisymmetric Downstream-Facing Step in Supersonic Flow." *AIAA Journal*, Vol. 4 No. 6, 975-980 1966.
- [31] Samimy, M., Petrie, H. L. and Addy, A. L. "A Study of Compressible Turbulent Reattaching Free Shear Layers." *AIAA Journal*, Vol.24 No. 2, February, 1986.
- [32] Schlichting, H. *Boundary-Layer Theory*. New York: McGraw-Hill, Inc. 7th ed., 1979.
- [33] Settles, G. S., Baca, B. K., Williams, D. R. and Bogdonoff, S. M. "A Study of the Reattachment of a Free Shear Layer in Compressible Turbulent Flow. *AIAA* paper 80-1408. Presented at the 13th Fluid and Plasma Dynamics Conference, Snowmass CO, July, 1980.
- [34] Shih, S. H., Hamed, A. and Yeuan, J. J. "Unsteady Supersonic Cavity Flow Simulations Using Coupled $k-\epsilon$ and Navier-Stokes Equations." *AIAA Journal*, Vol. 32 No10, 2015-2021, October, 1994.
- [35] Siegel, R. and Howell, J. R. *Thermal Radiation Heat Transfer*. Washington, DC: Taylor & Francis 3rd ed., 1992.
- [36] Stouffer, S. D. *The Effect of Flow Structure on the Combustion and Heat Transfer in a Scramjet Combustor*. Ph.D. Dissertation Virginia Polytechnic Institute and State University, July, 1995.
- [37] Tam, C.-J. and Disimile, P. J., "A Comparison of Several Standard Turbulence Models for 2-D Open Cavity Flow Field Computations." *AIAA* paper 95-0361. Presented at the 33rd Aerospace Sciences Meeting and Exhibit, January 9-12, 1995.
- [38] *The Temperature Handbook*. Stamford CT: Omega Engineering, Vol. 29, 1995.
- [39] Tishkoff, J. M., Drummond, J. P., Edwards, T. and Nejad, A. S. "Future Directions of Supersonic Combustion Research: Air Force/NASA Workshop on Supersonic Combustion." *AIAA* paper 97-1017.
- [40] Touloukian, Y. S. and Ho, C. Y., eds. *Thermophysical Properties of Matter*. Purdue University, Thermophysical Properties Research Center: IRI/Plenum Vol. 2., 1970.
- [41] Truitt, R.W. *Fundamentals of Aerodynamic Heating*. New York: The Ronald Press Company, 1960.
- [42] Van Driest, E. R. "Turbulent Boundary Layer in Compressible Fluids." *Journal of the Aeronautical Sciences*, Vol. 18 No. 3, 145-160 1951.
- [43] Weber, J. Program Manager, AFRL/PRSS, Wright-Patterson AFB OH. Personal communication. 1998.
- [44] —. Program Manager, AFRL/PRSS, Wright-Patterson AFB OH. Personal communication. 1998.

- [45] Weckesser, L. B. and Frazer, R. K. "Hypersonic Ramjet Materials Test." AD529274. October-December, 1973.
- [46] Weinberg, B. C., McDonald, H. and Shamroth, S. J. "Navier-Stokes Computations on Aft End Flow Fields." AD-A115 796/XAG, May, 1982.
- [47] Wheeler, A. J. and Ganji, A R. *Introduction to Engineering Experimentation*. Englewood Cliffs NJ: Prentice Hall, 1996.
- [48] White, F. M. *Fluid Mechanics*. New York: McGraw-Hill, Inc. 3rd ed., 1994.
- [49] White, F. M. *Viscous Fluid Flow*. New York: McGraw-Hill, Inc. 2nd ed., 1991.

Vita

Second Lieutenant Orval A. "Rusty" Powell was born on 10 September 1968 in Colorado Springs, Colorado. He graduated from Rampart High School in Colorado Springs in May, 1986. He completed one year of undergraduate studies at the University of Colorado at Colorado Springs before enlisting in the United States Air Force in August, 1988. He served for five years in the Air Force, at assignments located in Colorado, Germany and South Dakota, attaining the rank of Staff Sergeant. In July 1993, he separated from the Air Force upon accepting an AFROTC scholarship to attend Colorado State University, Fort Collins, Colorado. He graduated Summa Cum Laude with a degree in Mechanical Engineering in May, 1997 and was commissioned through Detachment 090, where he was recognized as a Distinguished Graduate.

In December, 1997, Rusty and his wife, Aimée Honour (Lerner) Powell, welcomed an addition to their family after nine years of marriage; they were blessed with a healthy baby girl, Jorrin Elizabeth.

The Air Force Institute of Technology was Rusty's first commissioned assignment. Upon graduation, he will be assigned to the Propulsion Directorate, Air Force Research Laboratory, Wright-Patterson Air Force Base, Ohio.

Permanent Address: 350 Taopi Circle

Woodland Park, CO 80863